

**$E1$  and  $E2$   $S$  factors of  $^{12}\text{C}(\alpha, \gamma)^{16}\text{O}$  from  $\gamma$ -ray angular distributions with a  $4\pi$ -detector array**

M. Assunção,<sup>1,\*</sup> M. Fey,<sup>2,†</sup> A. Lefebvre-Schuhl,<sup>1</sup> J. Kiener,<sup>1</sup> V. Tatischeff,<sup>1</sup> J. W. Hammer,<sup>2,‡</sup> C. Beck,<sup>3</sup> C. Boukari-Pelissie,<sup>1</sup> A. Coc,<sup>1</sup> J. J. Correia,<sup>1</sup> S. Courtin,<sup>3</sup> F. Fleurot,<sup>4,§</sup> E. Galanopoulos,<sup>5</sup> C. Grama,<sup>1,||</sup> F. Haas,<sup>3</sup> F. Hammache,<sup>6,¶</sup> F. Hannachi,<sup>1,\*\*</sup> S. Harissopulos,<sup>5</sup> A. Korichi,<sup>1</sup> R. Kunz,<sup>2,††</sup> D. LeDu,<sup>1</sup> A. Lopez-Martens,<sup>1</sup> D. Malcherek,<sup>2,‡‡</sup> R. Meunier,<sup>1</sup> Th. Paradellis,<sup>5,§§</sup> M. Rousseau,<sup>3</sup> N. Rowley,<sup>3</sup> G. Staudt,<sup>7</sup> S. Szilner,<sup>3,|||</sup> J. P. Thibaud,<sup>1</sup> and J. L. Weil<sup>8,¶¶</sup>

<sup>1</sup>Centre de Spectrométrie Nucléaire et de Spectrométrie de Masse (CSNSM), UMR8609, CNRS/IN2P3; Université Paris-Sud, F-91405 Orsay-Campus, France

<sup>2</sup>Institut für Strahlenphysik (IfS), Universität Stuttgart, D-70550 Stuttgart, Germany

<sup>3</sup>Institut Pluridisciplinaire Hubert Curien (IPHC), UMR7178, Département de Recherches Subatomiques, CNRS/IN2P3; Université Louis Pasteur (Strasbourg I), 23 rue du Loess, B.P. 28, F-67037 Strasbourg Cedex, 2, France

<sup>4</sup>Kernfysisch Versneller Instituut (KVI), University of Groningen, NL-9747 AA Groningen, Netherlands

<sup>5</sup>Institute of Nuclear Physics, N.C.S.R. Demokritos Athens, GR-15310 Athens, Greece

<sup>6</sup>Gesellschaft für Schwerionenforschung mbH (GSI), D-64291 Darmstadt, Germany

<sup>7</sup>Physikalisches Institut, Universität Tübingen, D-72076 Tübingen, Germany

<sup>8</sup>Institute of Isotopes, Hungarian Academy of Sciences, H-1525 Budapest, Hungary

(Received 30 June 2004; revised manuscript received 31 August 2005; published 11 May 2006)

A new experiment to determine the thermonuclear cross section of the  $^{12}\text{C}(\alpha, \gamma)^{16}\text{O}$  reaction has been performed in regular kinematics using an intense  $\alpha$ -particle beam of up to  $340\ \mu\text{A}$  from the Stuttgart DYNAMITRON. For the first time, a  $4\pi$ -germanium-detector setup has been used to measure the angular distribution of the  $\gamma$  rays at all angles simultaneously. It consisted of an array of nine EUROGAM high-purity Ge detectors in close geometry, actively shielded individually with bismuth germanate crystals. The  $^{12}\text{C}$  targets were isotopically enriched by magnetic separation during implantation. The depth profiles of the implanted carbon in the  $^{12}\text{C}$  targets were determined by Rutherford backscattering for purposes of cross-section normalization and absolute determination of the  $E1$  and  $E2$   $S$  factors. Angular distributions of the  $\gamma$  decay to the  $^{16}\text{O}$  ground state were measured in the energy range  $E_{\text{c.m.}} = 1.30\text{--}2.78$  MeV and in the angular range (lab.)  $30^\circ\text{--}130^\circ$ . From these distributions, astrophysical  $E1$  and  $E2$   $S$ -factor functions vs energy were calculated, both of which are indispensable to the modeling of this reaction and the extrapolation toward lower energies. The separation of the  $E1$  and  $E2$  capture channels was done both by taking the phase value  $\phi_{12}$  as a free parameter and by fixing it using the results of elastic  $\alpha$ -particle scattering on  $^{12}\text{C}$  in the same energy range.

DOI: [10.1103/PhysRevC.73.055801](https://doi.org/10.1103/PhysRevC.73.055801)

PACS number(s): 25.55.-e, 24.30.-v, 26.20.+f, 27.20.+n

## I. INTRODUCTION

$\alpha$ -particle capture on  $^{12}\text{C}$  is considered to be the most important thermonuclear reaction in nonexplosive astrophysical sites [1,2]. The  $^{12}\text{C}(\alpha, \gamma)^{16}\text{O}$  reaction rate enters directly as an important parameter in many stellar evolution models. This reaction follows the production of  $^{12}\text{C}$  by the triple- $\alpha$  process in stellar cores which have exhausted their hydrogen. The ratio of the thermonuclear reaction yields of these two reactions determines directly the carbon-to-oxygen ratio at the end of helium burning. Many later aspects of stellar evolution and nucleosynthesis are very sensitive to this parameter. For example, it influences the composition of white dwarfs. Also, in massive stars which ignite in further hydrostatic burning stages (carbon, neon, and oxygen burning, etc.), the abundance ratio of  $^{12}\text{C}$  to  $^{16}\text{O}$  has important consequences for the nucleosynthetic yield of many intermediate-mass isotopes which are almost exclusively produced in these stars [3,4]. In addition, the  $^{12}\text{C}(\alpha, \gamma)^{16}\text{O}$  reaction rate has an important influence on explosive burning and on the nucleosynthesis following a supernova event. Finally, it influences significantly the final state of massive stars: white dwarfs, neutron stars, or black holes [4]. Brown *et al.* showed the influence of the  $^{12}\text{C}(\alpha, \gamma)^{16}\text{O}$  rate on the formation of massive black holes [5,6], and they found a threshold of about  $20 M_\odot$  for the mass

\*Present address: Departamento de Física Nuclear of Instituto de Física da Universidade de São Paulo, São Paulo, SP, Brazil.

†Now at Robert Bosch GmbH, D-71701 Schwieberdingen, Germany.

‡Now at the Phys. Depart. Univ. of Notre Dame, USA.

§Now at the Laurentian University, Sudbury (Ontario), Canada.

|| Also at Institute of Physics and Nuclear Engineering, RO-76900 Bucharest Magurele, Romania.

¶Now at the Institut de Physique Nucléaire d'Orsay (IPN), UMR8608, F-91406 Orsay Cedex, France.

\*\*Now at the Centre d'Études Nucléaires de Bordeaux-Gradignan (CENBG) UMR5797, B.P. 120, F-33175 Gradignan Cedex, France.

††Present address: Experimentalphysik III-Physik mit Ionenstrahlen, Fakultät für Physik und Astronomie, NB 3/131, Ruhr-Universität Bochum (RUB), Universitätsstr. 150, D-44780 Bochum, Germany.

‡‡Now at the Institut für Technische Verbrennung, Universität Stuttgart, D-70550 Stuttgart, Germany.

§§Deceased.

||| Present address: Ruder Bosković Institute, HR-10 002 Zagreb, Croatia.

¶¶ Also at Dept. of Physics, University of Kentucky, Lexington, KY 40506, USA.

of the progenitors of the black holes using the recently assumed reaction rate [7]. For all these reasons,  $^{12}\text{C}(\alpha, \gamma)^{16}\text{O}$  is still considered the key reaction in nucleosynthesis.

In spite of its importance in astrophysics and several decades of intense experimental and theoretical efforts, the extrapolated reaction cross section or equivalently the astrophysical  $S$  factor of the  $^{12}\text{C}(\alpha, \gamma)^{16}\text{O}$  reaction at helium-burning temperatures ( $T \approx 2 \times 10^8$  K) is still uncertain by  $\pm 41\%$  according to the NACRE compilation [8] and by  $\pm 31\%$  according to recent work of Kunz *et al.* [9,10]. Depending on which stellar model is used, the required precision varies over a large range down to  $\pm 10\%$  at a  $2 \sigma$  limit for the study of nucleosynthesis in massive stars [4]. The cross section of  $^{12}\text{C}(\alpha, \gamma)^{16}\text{O}$  in the energy region of the corresponding Gamow window for helium burning around 300 keV is estimated to be of the order of  $10^{-41}$  cm<sup>2</sup>, with about equal contributions of  $E1$  and  $E2$  radiative capture. Since the direct measurement of such a low cross section is completely excluded given present experimental techniques, accurate cross-section measurements spanning a wide energy region, as low as possible above the Gamow window to constrain the theoretical extrapolation to astrophysical energies, still seem to be the best alternative.

Because of the nuclear structure of the nuclei involved (see [11]), broad and subthreshold  $1^-$  resonances, located at 2.424 and  $-0.045$  MeV, respectively (given in particle center-of-mass energies), are responsible for the  $E1$  capture component. The  $E2$  component is even more complicated, being affected by a subthreshold  $2^+$  resonance at  $-0.245$  MeV, the narrow  $2^+$  resonance at 2.683 MeV, and at least two known higher-lying resonances, all of which have to be considered, along with nonresonant capture and all possible interference effects [2,12]. The knowledge of both  $S$ -factor functions  $S_{E1}(E)$  and  $S_{E2}(E)$  is absolutely necessary for modeling and extrapolating the excitation functions into the energy range of stellar helium burning by means of the  $R$ - or  $K$ -matrix formalism.

In the last decade, much progress has been made in the determination of the  $E1$  part of the thermonuclear cross section, especially by including accurate new data for  $^{12}\text{C}(\alpha, \gamma)^{16}\text{O}$  and for the  $\alpha$ -particle spectrum following the  $\beta$  decay of  $^{16}\text{N}$ , and by performing  $R$ - or  $K$ -matrix fits to these data and to the phase shifts for elastic  $\alpha$ -particle scattering on  $^{12}\text{C}$  (see, e.g., Azuma *et al.* [13]). However, less progress has been made regarding the  $E2$  part, and the major uncertainty of the thermonuclear reaction rate at present is due to that component. The early work of Dyer and Barnes [14] was performed in direct kinematics with four movable NaI(Tl) detectors to get  $\gamma$ -ray angular distributions at four energies. Additional ground state measurements were performed at higher energies, in particular by Ophel *et al.* [15] for the  $E1$  capture amplitude from 6.5 to 8.5 MeV at  $\theta = 90^\circ$ . Kettner *et al.* [16] used inverse kinematics and two large NaI(Tl) detectors to measure total cross sections by studying direct and cascade  $\gamma$ -ray transitions to the ground state. Redder *et al.* [17] conducted an experiment at the Stuttgart DYNAMITRON using several different detector arrangements [eight NaI(Tl), six high-purity (HP) Ge, and three HPGe] to obtain angular distributions. The  $\alpha$ -beam currents were in the range of 700–800  $\mu\text{A}$ . This experiment yielded for the first time a clear indication that the

$E2$  component has about the same strength as the  $E1$  and that it therefore cannot be neglected. In inverse kinematics, with a recoil separator and large NaI(Tl)  $\gamma$ -ray detectors, Kremer *et al.* [18] extracted the  $E1$  values by subtracting out the  $E2$  component based on previously published results [14,17]. Ouellet *et al.* [19,20] performed an investigation similar to the work of Redder *et al.* [17] by using six large-volume Ge detectors located at five different angles and an improved target technique, but much lower  $\alpha$ -beam currents in the range 30–35  $\mu\text{A}$ . The first evaluation of this experiment yielded extremely low  $S$  factors [19], which were corrected in a second paper [20]. To obtain high efficiency for  $\gamma$ -ray detection, Rogalla [21] conducted an experiment using a summing crystal, the first  $4\pi$  experiment for this reaction, but without angular information. In a subsequent two-detector experiment at DTL Bochum, Trautvetter *et al.* [22] and Roters *et al.* [23] disentangled the  $E1$  and  $E2$  components by rather complicated procedures because the large detector used summed up the two angular distributions of  $E1$  and  $E2$ . In the experiment of Kunz *et al.* [9], the angular distributions were measured sequentially by using an array of three or four detectors in a fixed relative geometry which could be moved into three different positions to obtain nine angular data points. In this way, a higher detection efficiency was obtained. Gialanella *et al.* [24] concentrated on the measurement of the  $E1$  component by using a ring of Ge detectors at  $90^\circ$  and at a rather large distance from the helium gas target. This experiment was done in inverse kinematics. Tischhauser *et al.* [25] undertook a new and refined measurement of the elastic scattering of  $\alpha$  particles on  $^{12}\text{C}$  to obtain information on the nuclear levels involved and to extract information on the  $S$  factors. Very recently, D. Schürmann *et al.* [26] measured the total cross section of the reaction in inverse kinematics using the recoil mass separator ERNA in combination with a windowless He gas target in the energy range between 1.9 and 4.9 MeV.

Besides the direct investigations of this reaction, several indirect experimental determinations have been performed. Two of them yield significant new information: the measurement of the  $\beta$ -delayed  $\alpha$  decay of  $^{16}\text{N}$  [13] and an experiment using subcoulomb  $\alpha$  transfer for the study of the  $^{12}\text{C}(\alpha, \gamma)^{16}\text{O}$  reaction [27,28].

Considering all these efforts, we concluded that the extraction of the  $E2$  component can best be done by accurate angular distribution measurements of the capture  $\gamma$  rays in regular kinematics. We limited our study to the ground state transitions which are believed to give the major contribution to  $S(300)$  [10,16,17]. Such angular distributions have already been obtained in several other investigations as mentioned above, but the accuracy of the astrophysical  $E2$   $S$  factor was always limited by either the number of angular data points, the spectral quality, or the beam intensity. Another important piece of information in such measurements is knowledge of the effective target thickness and the target profile, which requires the use of solid state physics techniques.

We report here on a new measurement of the low-energy cross section of the  $^{12}\text{C}(\alpha, \gamma)^{16}\text{O}$  reaction for  $\alpha$ -particle beam energies between 1.850 and 3.730 MeV. The experiment was performed at the Stuttgart DYNAMITRON accelerator, aiming especially at an accurate determination of the  $\gamma$ -ray angular

distributions by the use of a  $4\pi$  HPGe detector array with active bismuth germanate (BGO) shielding in close geometry. This experiment was the fourth in a long series of experiments [9,17,29,30] undertaken at the Stuttgart DYNAMITRON laboratory to explore the  $^{12}\text{C}(\alpha, \gamma)^{16}\text{O}$  reaction and to develop the required experimental and numerical techniques.

Experimental techniques and details of the experiment with the  $4\pi$ -detector array will be given in Sec. II. With this  $4\pi$  setup, we obtained low-background spectra simultaneously at nine angles in the range  $30^\circ - 130^\circ$  (lab.), with small systematic errors in the angular distribution data due to the fixed geometry. The  $^{12}\text{C}$  depth profiles of the targets were obtained with the Rutherford backscattering (RBS) technique as presented in Sec. III. In the data analysis described in Sec. IV, the profiles were taken into account after making the two- or three-parameter cross-section fits to the  $\gamma$ -ray angular distributions, which either took the  $E1$ - $E2$  phase  $\phi_{12}$  as a free parameter or calculated it from the elastic scattering data of Plaga *et al.* [31] for the low-energy range and of D'Agostino Bruno *et al.* [32] for the higher energy range. All of this allowed us to extract accurate astrophysical  $S$  factors for the  $E1$  and  $E2$  components over the whole measured energy range, and especially for the  $E2$  component around the broad  $E1$  resonance at 2.42 MeV, where the cross-section ratio  $\sigma_{E2}/\sigma_{E1}$  is very small. The results obtained with the two methods are presented in tabular form and compared with other measurements. Some discussion of the importance of the carbon depth profile is also given. Finally, our conclusions are proposed in Sec. V.

## II. THE EXPERIMENT

For the measurement of extremely low cross sections as in the case of the  $^{12}\text{C}(\alpha, \gamma)^{16}\text{O}$  reaction, the four essential ingredients defining the experimental sensitivity have been optimized as far as possible: beam intensity, detector efficiency and quality, target layer and quality, and measuring time.

### A. Accelerator and beam transport

The experiment was performed at the Stuttgart DYNAMITRON accelerator in the energy interval  $E_{\alpha, \text{lab}} = 1.850 - 3.730$  MeV. The  $^4\text{He}^+$ -beam intensity was in the range  $100 - 340 \mu\text{A}$ . The runs at voltages above 3.3 MeV had to be carried out with reduced beam currents.

The beam transport system [33,34], which is pumped entirely by turbomolecular pumps to a vacuum of typically  $2 \times 10^{-7}$  mbar, keeps the contamination from hydrocarbons rather low. In order to maintain ultimate purity around the target, four cryotrap at liquid nitrogen temperature were used. Three of them were located in the beam pipe coaxial with the beam axis in front of the target. The traps were made from gold-plated copper tubes of 35 mm diameter with a length of about 1 m each, providing a surface sufficiently large to trap the residual contaminants very effectively. Two main reasons dictated our choice of the gold plating: first it reduced the  $\gamma$ -ray background in the energy range of interest, and second high-purity gold is available and it has a good thermal conductivity. The fourth trap was located directly above the turbomolecular pump which evacuated the target zone to avoid contamination also at this stage. The last section

of the beam pipe could be exchanged together with the target to regenerate the last cryotrap during target replacement, thus enabling off-line preparation of a new target and its connected cryotrap. Further details are described in Kunz [35], where some relevant drawings are also shown.

### B. Enriched $^{12}\text{C}$ targets for high beam powers

The target constructed for high beam powers was a variant of one used in previous experiments [9,17,36–38], and it was tested for beam loads of up to  $10 \text{ kW/cm}^2$ . The new variant could be turned around without breaking vacuum to make realistic background measurements on the nonimplanted reverse side of the backing which had been constructed to be the same as the implanted front side. This design enabled us to make differential measurements of the reaction yield, subtracting not only the background from the environment but also a major part of the beam-induced background. A photo of the target is shown in Fig. 1. The cooling of the target backing



FIG. 1. Target designed for high beam powers of up to  $10 \text{ kW/cm}^2$ . The backing consists of a 2 mm thick copper plate with 14 one mm diameter cooling channels covering an area of about  $25 \times 25 \text{ mm}^2$ . Cooling water flowed at about 25 m/s with a pressure of 50 bars. The backing is soldered into a stainless steel cylinder that enables connecting the water and reversing the target without breaking vacuum. The copper plate was plated with a layer of  $20 \mu\text{m}$  of high-purity gold, serving as the substrate for the  $^{12}\text{C}$  implantation.

[36], which was made from oxygen-free high-conductivity (OFHC) copper and was only 2 mm thick, was achieved by water flowing through 14 tiny channels inside the backing at a flow velocity of typically 25 m/s and a pressure of about 50 bars. The high flow gives an efficient heat transfer from metal to water, and the high pressure shifts the boiling point of the water to 263°C, preventing target burnout that would be caused by the reduced heat transfer resulting from vapor bubbles in the cooling channels. The surface temperature of the target was less than 180°C for a uniformly distributed beam current density of less than 10 kW/cm<sup>2</sup>. The target backing was gold plated on both sides for the same reason as for the cryotrap tubes. The gold platings were produced by a company<sup>1</sup> specializing in a noble metal galvano technique. The 20 μm gold layer thickness is sufficient to stop all particles in this layer. Despite some troubles due to the high diffusibility of particles inside gold, it remains a good substrate for the implantation of carbon. Tests with other platings with lower particle diffusibility, as, for instance, nickel, yielded a higher beam-induced background caused by the impurities of the layer.

The target consisting of enriched <sup>12</sup>C was produced by ion implantation using implanters of the DYNAMITRON Tandem Laboratory of the University of Bochum and the SIDONIE implanter of the CSNSM of Orsay. The geometry of the backing and the consequent deformation of the electric field did not allow a deposition of carbon on the surface of the gold layer with a very low energy, even though that would have been the ideal technique. Thin targets are more appropriate for the study of the vicinity of the narrow *E*2 resonance where the cross section varies rapidly, while quite thick targets are needed to get sufficient counts in the energy range located well below the *E*1 resonance where the cross section is very small. Implantations were performed at two energies: 70 keV for the Bochum targets and 20 keV for the Orsay targets. The lower implantation energy permitted building up thinner carbon layers within the backing nearer the surface. With higher ion beam energies, five to ten times thicker targets were made, but with a deeper distribution in the gold backing. There is no advantage in increasing the target thickness beyond about 10<sup>19</sup> atoms/cm<sup>2</sup> because the drop in the cross section with decreasing  $\alpha$  energy has the consequence that only the surface layer contributes significantly to the reaction yield.

<sup>13</sup>C in the target is unwanted because the normalized reaction yield of the reaction <sup>13</sup>C( $\alpha$ , *n*)<sup>16</sup>O is about five orders of magnitude higher than the <sup>12</sup>C( $\alpha$ ,  $\gamma$ )<sup>16</sup>O reaction yield at the relevant energies. The <sup>13</sup>C contamination is due to two contributions. The first is the natural carbon content in the volume of the gold layer which cannot be further reduced with the present techniques (heating the gold-plated backings under vacuum before implantation and subsequent continuous storage under argon before and after implantation). Because of the smaller amounts of implanted carbon, the gold-plated backings were heated on the Orsay targets; but heating was not necessary with the Bochum targets, for which the natural carbon amounts in the gold layer were negligible compared to

the thick implanted amounts. The second contribution comes from the carbon implantation process itself. Separation of the carbon isotopes with mass 12 (natural abundance 98.90%) and 13 (natural abundance 1.10%) was done by the usual magnetic separation of the beam. Depletion of the <sup>13</sup>C was thus improved overall. The magnetic separation technique alone is able to produce a <sup>12</sup>C layer depleted to a high degree, possibly by five orders of magnitude. All in all, the remaining <sup>13</sup>C contamination did not affect significantly the  $\gamma$  spectra in the studied energy range. <sup>12</sup>C was implanted into only one side of the backing, leaving the identical other side free for background measurements.

The thickness of each target was measured using the <sup>12</sup>C(*p*,  $\gamma$ )<sup>13</sup>N resonance at  $E_p = 1.69$  MeV. The resonance at 1.75 MeV of the reaction <sup>13</sup>C(*p*,  $\gamma$ )<sup>14</sup>N was also used for checking the original condition and time evolution of the thicker Bochum targets. These resonance studies allowed us to measure the <sup>13</sup>C depth profile in the implanted carbon layer as well as in the remaining gold layer. We found that in the implanted layer, the amount of <sup>13</sup>C due to the natural carbon content of the gold-backing layer was negligible compared to the implanted <sup>13</sup>C amount. Hence, it was possible to assume the same depth profiles for <sup>12</sup>C and residual <sup>13</sup>C in the implanted carbon layer. These measurements verified that there was a negligible buildup of carbon on the target surfaces during the course of the  $\alpha$ -particle bombardment. Because we used the <sup>12</sup>C(*p*,  $\gamma$ )<sup>13</sup>N resonance and the RBS measurements described in Sec. III to determine the <sup>12</sup>C depth profile, we employed the <sup>13</sup>C measurements mainly as in-beam determinations of the evolution of the target during its  $\alpha$ -beam exposure. Additional checks were also performed continuously during the experiment by measuring the time evolution of the intensities of the well-known broad, low-energy  $\gamma$  rays due to the (*n*, *n'*) $\gamma$  reactions on the germanium nuclei of the detectors.

For the (*p*,  $\gamma$ ) resonance studies, the DYNAMITRON accelerator had to be switched quickly from an  $\alpha$ -particle beam to a proton beam and vice versa. Yield checks had to be made at intervals of 1–2 days. Another check using the 2<sup>+</sup> resonance of <sup>12</sup>C( $\alpha$ ,  $\gamma$ )<sup>16</sup>O at  $E_{c.m.} = 2.68$  MeV was possible only once during the beam time period because of the difficulties in keeping the required high voltage and in quickly changing the particle energy. Typical target layers contained  $1.3 \times 10^{18}$  <sup>12</sup>C atoms/cm<sup>2</sup> for the thinnest targets and  $6\text{--}11 \times 10^{18}$  <sup>12</sup>C atoms/cm<sup>2</sup> for the thickest ones. Some targets with about  $0.5 \times 10^{18}$  <sup>12</sup>C atoms/cm<sup>2</sup> were also used in the energy range between the 1<sup>-</sup> and the 2<sup>+</sup> resonance. A target thickness value is given later in Table II for each effective center-of-mass (c.m.) energy.

In order to measure the cross section at energies around the narrow 2<sup>+</sup> resonance and around the broad 1<sup>-</sup> resonance, on the one hand, and in the energy range well below the 1<sup>-</sup> resonance on the other hand, targets with  $1.3 \times 10^{18}$  atoms/cm<sup>2</sup> were used for the 2<sup>+</sup> and the 1<sup>-</sup> resonances, and with  $6\text{--}11 \times 10^{18}$  atoms/cm<sup>2</sup> for the low energy range. The targets were replaced during the <sup>12</sup>C( $\alpha$ ,  $\gamma$ )<sup>16</sup>O measurement, before significant deterioration by the intense  $\alpha$ -particle beam occurred, i.e., before the amount of <sup>12</sup>C decreased by 20% at any one beam energy. Frequent checks of the target deterioration were done as described above. In addition, for

<sup>1</sup>Umicore Galvanotechnik GmbH, the former Demetron-Degussa company, Schwäbisch Gmünd, Germany.

each beam energy, the target thickness decrease could be monitored by the counting rate of the capture  $\gamma$  rays of 8–10 MeV. The effective target thickness ranged from 164 keV at  $E_{\alpha,\text{lab}} = 1.850$  MeV for the thick targets with  $11 \times 10^{18}$  atoms/cm<sup>2</sup> to 34 keV at 3.730 MeV for the thin targets with  $1.3 \times 10^{18}$  atoms/cm<sup>2</sup>. One has to be aware that the energy loss is caused by the mixture of carbon and gold. Additional post-irradiation checks of the target deterioration and homogeneity were performed by the RBS technique and are described in Sec. III. These RBS analyses showed some sputtering, but allowed us to conclude that the evolution of the targets during bombardment was mainly due to diffusion processes (see later in Figs. 7 and 8). They also showed, as did examination under the microscope, that other deteriorating phenomena such as blistering and subsequent exfoliation seldom occurred. In the cases when they did, this deterioration was taken into account in the error bars.

### C. $4\pi$ -detector array

The angle-integrated or total cross section of  $^{12}\text{C}(\alpha, \gamma)^{16}\text{O}$  is about 100 pb at  $E_{\alpha,\text{lab}} = 2.0$  MeV, 10 pb at  $E_{\alpha,\text{lab}} = 1.5$  MeV, and 1 pb at  $E_{\alpha,\text{lab}} = 1.2$  MeV ( $E_{\text{c.m.}} = 0.9$  MeV). These small cross sections suggest the use of a detector array with the highest possible efficiency, full  $4\pi$  space coverage, and sufficient granularity to measure the angular distribution of the  $\gamma$  rays. The latter information is crucial to the separation of E1 and E2 transitions and to obtaining the necessary excitation functions for modeling the reaction in the  $R$ -matrix formalism. As a close approach to this ideal array, setups of 9 or 15 detectors were conceived and drafted, but finally the setup with 9 detectors was realized, which provided the tightest possible arrangement. The detectors, from the EUROGAM Collaboration<sup>2</sup> [39–41], were HPGe detectors surrounded by individual active shields made of BGO scintillators. Figure 2 shows a photo of the setup. The distance of any detector to the center of the target was about 13 cm. The relative efficiency of each of the nine detectors was typically 70% compared to a standard  $3'' \times 3''$  NaI detector.

A modular mechanical frame was designed and built as shown in Fig. 3. It consisted of three separate support systems, each holding three detectors. Each support could be moved along a track perpendicular to the beam axis to give quick access to the detectors and the target zone. This feature is shown in Fig. 3(b), where the three supports have been moved away from the target. Changing the target could be done in a few minutes. After a target exchange, the measuring position again was reproduced with precise end stops, thus fixing the geometry of the detectors for the whole experiment. Each individual support was constructed as a ring which could be turned within certain limits to adjust the angular position of the detectors. The detectors were arranged in the following angular positions relative to the beam:  $30^\circ$ ,  $48^\circ$ ,  $60^\circ$ ,  $70^\circ$ ,  $83^\circ$ ,  $90^\circ$ ,  $111^\circ$ ,  $120^\circ$ , and  $130^\circ$ . These angular positions were determined using standard mechanical

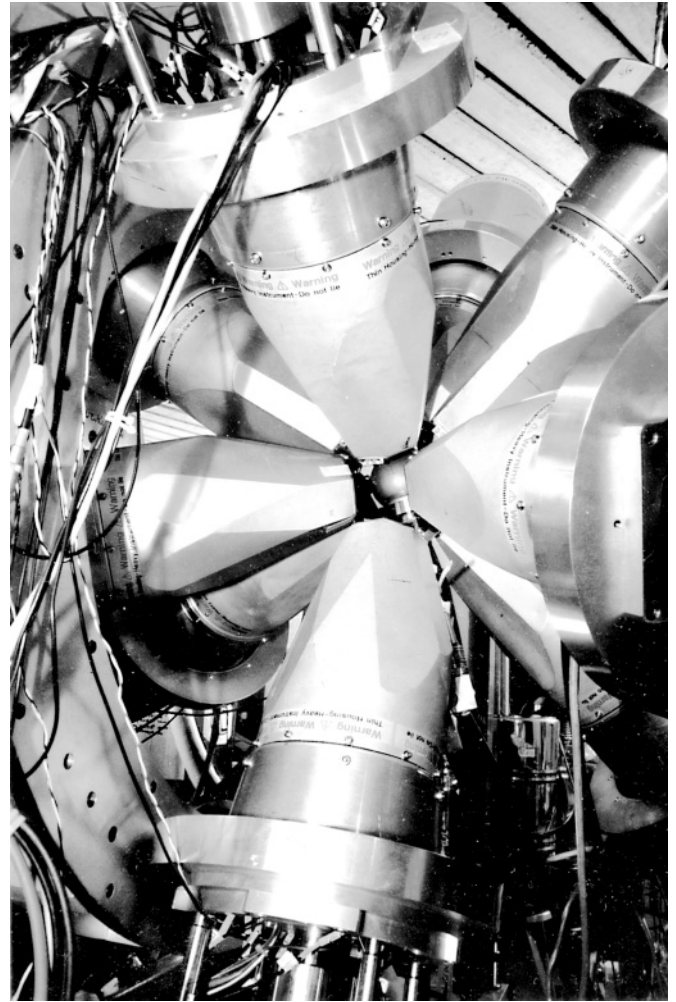


FIG. 2. View of the central part of the  $4\pi$ -detector setup consisting of nine EUROGAM detectors in close geometry with the target in the center of the array in a small spherical vacuum chamber.

techniques with an overall uncertainty of  $0.5^\circ$ , taking into account the periodic repositioning of the frames as well as the mechanical deformation of each frame when setting the detectors on the frame or adding their liquid nitrogen coolant. Small shifts of the beam impact point on the target were sometimes observed. This effect was always smaller than  $2.5^\circ$  at any of the detection angles. The influence of such beam impact shifts on the angular distribution fits was studied and is included in the error bars on the tabulated cross-section values.

### D. Calibrations and background subtraction

$^{56}\text{Co}$  and  $^{60}\text{Co}$  standard sources were used for energy calibrations and absolute efficiency measurements. For the highest  $\gamma$  energies, the  $^{27}\text{Al}(p, \gamma)^{28}\text{Si}$  reaction [42,43] was used for the same purposes and in the geometry of the  $^{12}\text{C}(\alpha, \gamma)^{16}\text{O}$  measurements. Because of the overlap of the energy ranges covered by the sources and the  $^{27}\text{Al}(p, \gamma)^{28}\text{Si}$  reaction, the absolute efficiencies were obtained as a function of energy by a least-squares fit to the data using for the energy dependence of the efficiencies, a known function found to fit with high

<sup>2</sup>The Ge detectors and their BGO shields were loaned to us by the IN2P3-EPSC France-UK Gamma-Ray Loan Pool.

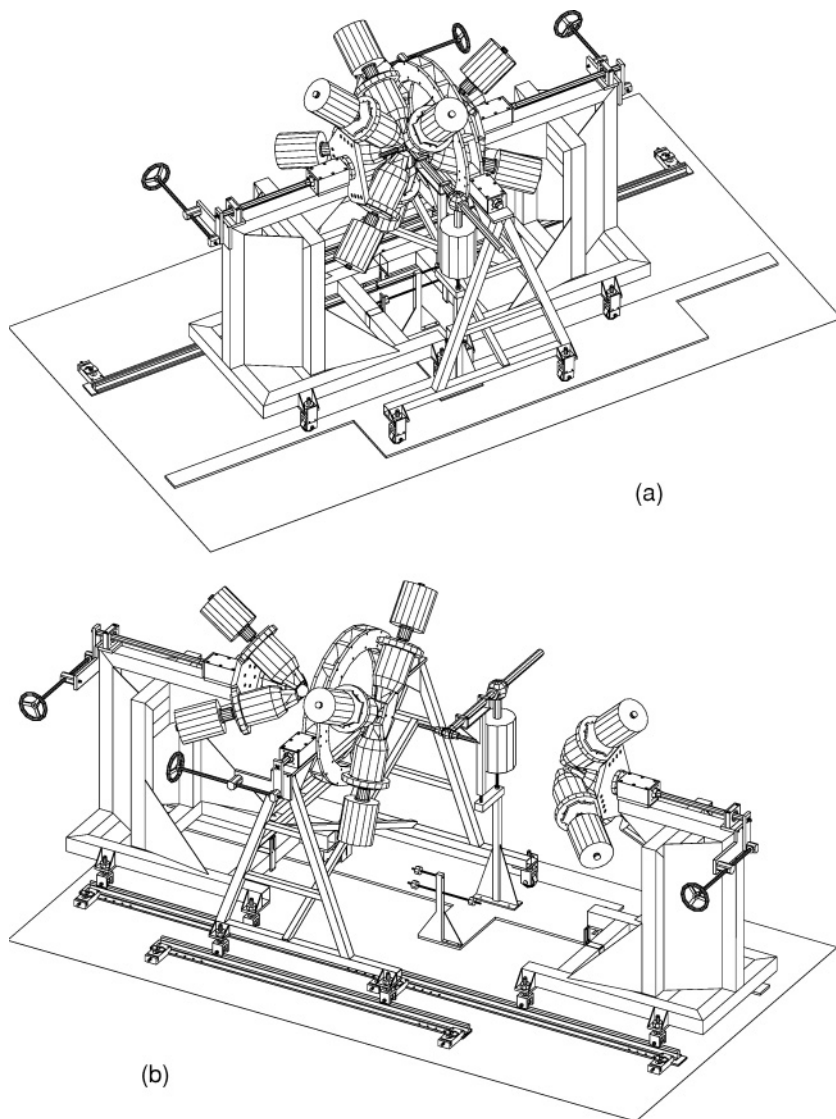


FIG. 3. Drawings of the setup used to measure  $\gamma$ -ray angular distributions of the  $^{12}\text{C}(\alpha, \gamma)^{16}\text{O}$  reaction in the measuring configuration (a) and in the service position (b) with dispersed supports and easy access to target and detectors. Three separate supports were used to hold the detectors in groups of three. These three supports could be moved on tracks for easy access to the target and all parts of the detectors. Rotation of the supports allowed setting the angular positions within certain limits.

precision in previous experiments with these Ge detectors. This method gave an absolute efficiency function over the whole studied energy range for each individual detector. Hence each detector could be considered as independent, and the uncertainties in the relative efficiency between detectors could be considered as statistical. The overall statistical uncertainty of each detector's efficiency function was 5%. Only the uncertainty in the absolute activity of the sources is a systematic uncertainty (less than 2%). As this uncertainty acts as a multiplicative factor for each point of the angular distribution, it should be directly transmitted to the cross-section and  $S$ -factor uncertainties, but it would not affect the angular distribution shape. In the following, we did not take into account this 2%, which was negligible compared to the uncertainties coming from the angular distribution fits. The absolute efficiency of a single detector at 10 MeV was in the range  $0.7\text{--}2.1 \times 10^{-4}$ , depending on the detector. The large variation is principally due to the  $\gamma$  absorption of the target holder.

In the  $^{12}\text{C}(\alpha, \gamma)^{16}\text{O}$  experiment, one is confronted not only with Doppler broadening and shifting of the capture  $\gamma$ -ray lines, but also with several sources of background

radiation. The capture lines are further broadened due to the target thickness, both effects summing up to a typical line width of 20–70 keV depending on the target thickness and on the energy of the incident  $\alpha$  particles. Nevertheless, the high resolution of the Ge counters is useful because one always has a rather high and unavoidable background from the beam. In particular, neutrons cause sharp capture lines in the energy range 5–11 MeV. Using Ge counters instead of scintillation detectors, these background lines superimposed on a broad  $\gamma$ -ray reaction line can be identified and separated in a refined analysis. For all the targets, the low  $^{13}\text{C}$  contamination was confirmed throughout the whole experiment using the  $^{13}\text{C}(p, \gamma)$  reaction. The contribution of the gold layer to the background spectra was measured by bombarding the side with the pure gold layer for each new target and each new beam energy. The background spectra, appropriately normalized, were then subtracted from the reaction spectra. In addition to the neutron capture lines, there is a Compton continuum related to all lines which can bury the desired reaction lines. The BGO detectors are helpful in reducing this background continuum. A reduction factor of up to 40 in the studied energy

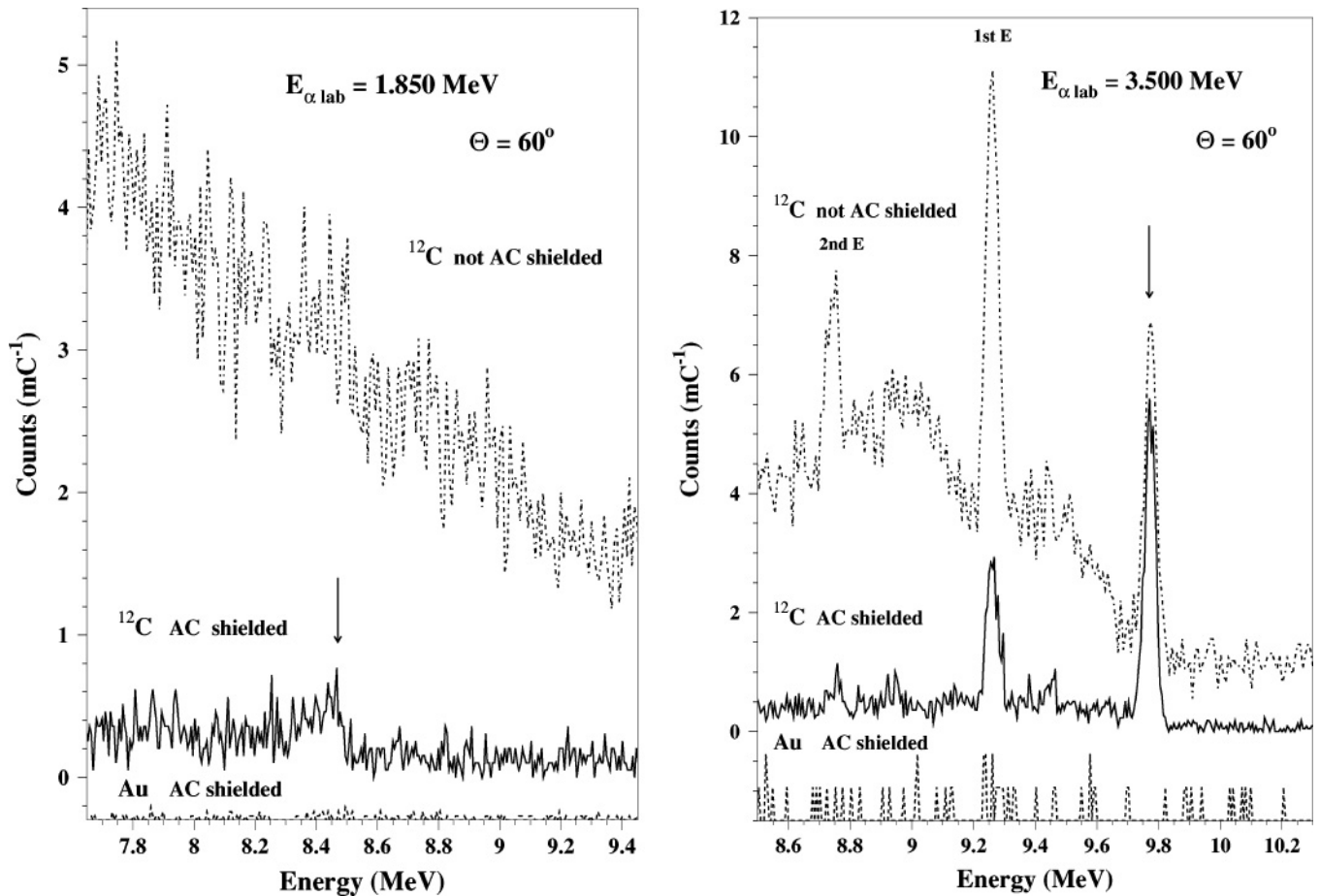


FIG. 4.  $\gamma$ -ray spectra of the  $^{12}\text{C}(\alpha, \gamma)^{16}\text{O}$  reaction registered at  $60^\circ$  for  $E_{\alpha, \text{lab}} = 1.850$  MeV, the lowest energy in this experiment, and  $E_{\alpha, \text{lab}} = 3.500$  MeV. Top spectra were taken without Compton suppression, i.e., no active shielding. Middle spectra correspond to those with active shielding. Bottom spectra represent the background measured with the beam on the bare gold backing. AC means Compton suppression. For better clarity, the two lower spectra are shifted by  $-0.3$  and  $-1.5$  on the y axis. Peaks of interest are indicated by arrows. Symbol 1st E (2nd E) indicates the first (second) escape peak. All spectra are normalized to the accumulated charge (counts per millicoulomb of  $\alpha$ -particle beam).

range, i.e., between 8 and 11 MeV, is obtained for a pure cosmic-ray-induced background under no-beam conditions. The reduction decreases with the beam on target because of the increase of beam-induced background, principally caused by  $(n, \gamma)$  reactions, and it depends on the beam energy,  $\gamma$ -ray energy, and detection angle. A reduction factor of 5–15 in the region of the high-energy  $\gamma$  rays was possible with the beam on target for a detector at  $60^\circ$ , as shown in Fig. 4. (Note the suppressed zeros in the drawings.) This reduction is much better than with plastic Compton-suppression detectors [44] and was very helpful in extending the measurements to lower bombarding energies.

Some typical  $\gamma$ -ray spectra are shown in Fig. 4 for two energies: one was measured in the region between the E1 and the E2 resonance energies ( $E_{\alpha, \text{lab}} = 3.500$  MeV) and the other corresponds to the lowest energy reached during the experiment ( $E_{\alpha, \text{lab}} = 1.850$  MeV). The corresponding effective c.m. energies were 2.607 and 1.310 MeV. The calculation of the effective c.m. energy is described in Sec. III and takes into account the energy loss as well as the  $^{12}\text{C}$  profile in the target.  $E_{\alpha, \text{lab}}$  indicates the beam energy before applying the corrections for energy loss and target thickness.

The low level of the background as well as the high efficiency of the BGO shields appear clearly.

### E. The $^{12}\text{C}(\alpha, \gamma)^{16}\text{O}$ experiment

Angular distributions were measured at 25 energies between  $E_{c.m. \text{ eff.}} = 1.310$  and 2.780 MeV (see below). These measurements included the broad  $1^-$  resonance at  $E_{c.m.} = 2.42$  MeV and the region around the narrow  $2^+$  resonance at  $E_{c.m.} = 2.68$  MeV as well as several data points in the energy region below these resonances to determine the influence of subthreshold resonances. The results were corrected for the detector efficiencies to obtain the angular distributions. The nine  $\gamma$ -ray spectra registered at  $E_{\alpha, \text{lab}} = 3.500$  and 1.850 MeV are presented in Figs. 5 and 6.

After the measurement campaign at the Stuttgart DYNAMITRON, we investigated the  $^{12}\text{C}$  concentration, thickness, and homogeneity of the targets by RBS analyses (see Sec. III). Some targets were also checked before the experiment, which allowed determining their initial thicknesses and their homogeneity, both in  $^{12}\text{C}$  atomic density and depth profile on each point of the target. Furthermore, during

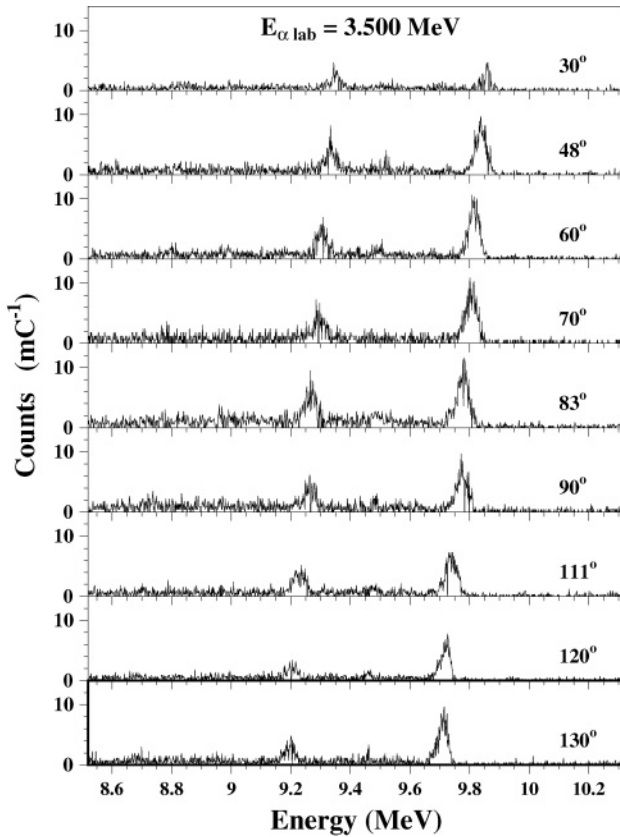


FIG. 5.  $\gamma$ -ray spectra of the  $^{12}\text{C}(\alpha, \gamma)^{16}\text{O}$  reaction for  $E_{\alpha, \text{lab}} = 3.500$  MeV ( $E_{\text{c.m. eff.}} = 2.607$  MeV) as a function of angle. To the left of the full energy peak, the single escape peak is clearly visible, but the double escape peak is almost completely suppressed by the active shielding. The spectra have been normalized to the accumulated charge (counts per millicoulomb of  $\alpha$ -particle beam) and to the efficiency of each Ge detector. The Doppler shift in the  $\gamma$  energy is clearly visible.

the DYNAMITRON runs, the  $^{12}\text{C}$  content was repeatedly determined by scans over the  $^{12}\text{C}(p, \gamma)^{13}\text{N}$  resonance at  $E_p = 1.699$  MeV. The results of these measurements agreed generally within the error bars with the RBS determinations. However, there were some exceptions when the two methods gave significantly different results. RBS analysis over the whole surface of the target (see below) showed that in these cases the proton and the  $\alpha$ -particle beams probably hit different areas of the target. For the analysis, we decided therefore to use exclusively the results of the RBS scans which covered the whole target areas and which were also more precise.

### III. ANALYSIS OF THE TARGETS BY RBS; EFFECTIVE REACTION ENERGIES

For RBS,  $\alpha$ -particle backscattering at an energy of  $E_{\alpha, \text{lab}} = 1.20$  MeV was chosen. The  $\alpha$ -particle beam was provided by the ARAMIS accelerator of the CSNSM Orsay. The backscattered particles were detected with a surface barrier detector at  $\theta = 165^\circ$  with respect to the beam. The target was scanned in a device with full automatic positioning under computer control, considerably reducing the required

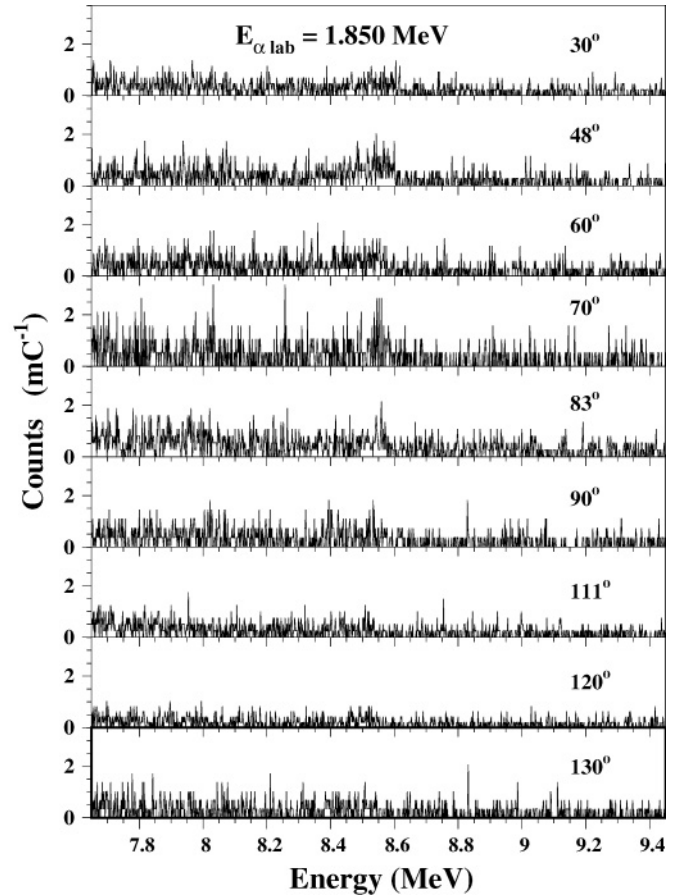


FIG. 6.  $\gamma$ -ray spectra of the  $^{12}\text{C}(\alpha, \gamma)^{16}\text{O}$  reaction for  $E_{\alpha, \text{lab}} = 1.850$  MeV ( $E_{\text{c.m. eff.}} = 1.305$  MeV), the lowest beam energy of this experiment in the angular range  $30^\circ$ – $130^\circ$  measured with the nine EUROGAM detectors. Full energy  $\gamma$  peak is around 8.56 MeV. Spectra have been normalized to the accumulated beam charge and to the efficiency of each Ge detector.

measuring time. For each target, a  $^{12}\text{C}$  depth profile was obtained at typically 30 different points with about half of the points inside the region of the beam impact zone and the other half outside that region. The points were selected using digitized images of the targets, which took into account the appearance of the target in and out of the beam impact zone. The target appearance clearly identified the interface between the regions as well as the unbombarded border of the target. The beam time for measuring one target to determine the average depth profile and homogeneity was approximately 6 h. Figure 7 shows typical RBS spectra observed for a target having  $1.3 \times 10^{18}$   $^{12}\text{C}$  atoms/cm<sup>2</sup> implanted in gold. The two spectra correspond to a central point of the target region where the DYNAMITRON beam produced the highest wear and to a region that had not been touched by the beam. The erosion of the  $^{12}\text{C}$  layer at the surface and the diffusion of carbon into the deeper gold layers are clearly visible. Each experimental RBS spectrum obtained was analyzed using the RBS analysis program RUMP [45]. The empirical fit to the experimental spectra gave the carbon depth profile in the gold layer. This information was later used to calculate the  $^{12}\text{C}$  concentrations and to determine the effective  $\alpha$ -particle energies for all runs of

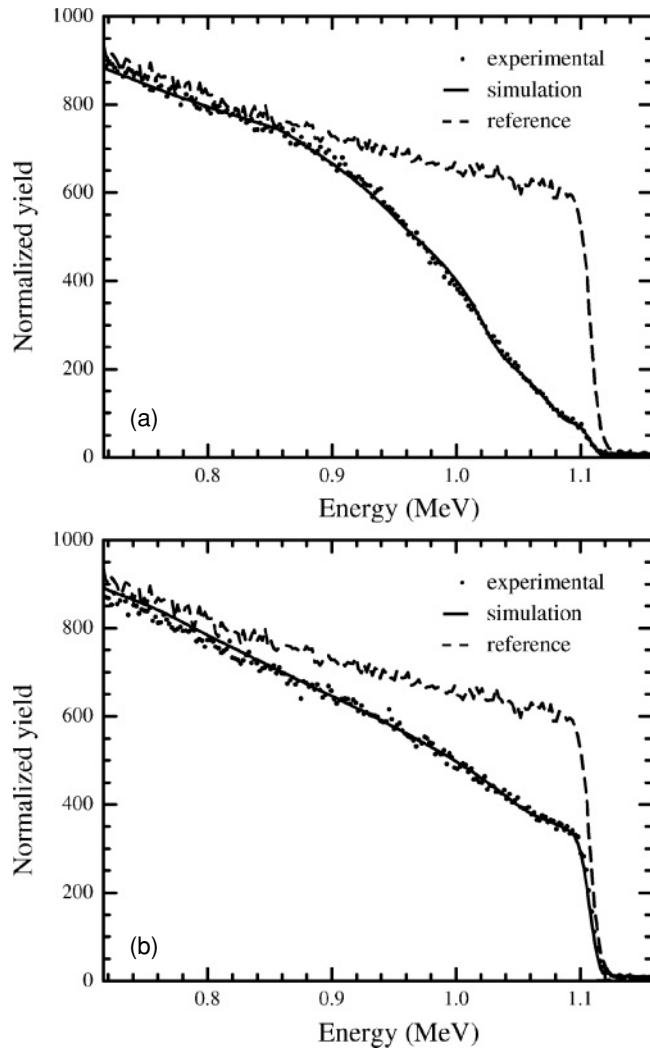


FIG. 7. Two RBS energy spectra for a  $^{12}\text{C}$  target using an analyzing beam of the ARAMIS accelerator of 1.20 MeV. (a) Target spectrum taken off center at a point of the target not hit and degraded by the high current beam. (b) Target spectrum at a point at the center of the target where some degradation took place. Full lines indicate simulated spectra obtained with the RUMP code [45]. Dashed lines give the reference spectrum obtained with a bare gold backing.

the  $^{12}\text{C}(\alpha, \gamma)^{16}\text{O}$  measurements. Figure 8 presents resulting depth profiles of the  $^{12}\text{C}$  concentration in the target before and after bombardment. Figure 9 gives the variation of the number of  $^{12}\text{C}$  atoms as a function of the position on a similar target at the end of the experiment.

In a real experiment, one cannot expect such ideal conditions as pointlike targets and detectors nor targets with zero energy loss of the particles. So the laboratory energy is the particle energy as it leaves the accelerator, and the effective reaction energy is smaller because of the energy loss in the target layer, and it is smeared out by the energy straggling because of the finite thickness of the target. In this paper, we are using effective energies as the closest approximation to the ideal conditions for the  $^{12}\text{C}(\alpha, \gamma)^{16}\text{O}$  measurements.

The effective reaction energy can be calculated by considering the average depth profile of  $^{12}\text{C}$  in the gold and the

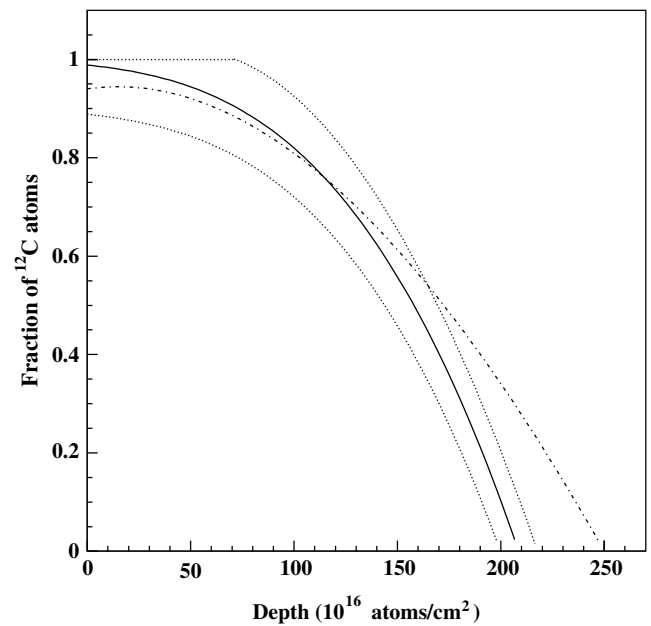


FIG. 8. Two examples of  $^{12}\text{C}$  depth profiles in the target deduced from RBS measurements. Full line is the profile before the  $\alpha$ -beam bombardment of the target; dotted lines are the limits (taken as  $\pm 10\%$ ; limited at 1 to maximum and 0 for the minimum) used to calculate the error bar on the initial effective energy. Dot-dashed line is a typical profile under the beam spot used to calculate the final thickness of the target and the final effective energy after bombardment. The same kind of limits was used to calculate the error bar on the final effective energy, but the two corresponding limit curves are not presented here, to simplify the figure. Depth unit is usual in such studies. The vertical scale is the ratio of the number of  $^{12}\text{C}$  atoms to the total number of  $^{12}\text{C}$  plus Au atoms at each depth inside the target.

$\alpha$ -particle energy losses associated with that depth profile. In the case of implanted carbon, one also needs the depth-dependent stoichiometry of the mixture of target atoms with the backing atoms. Moreover, knowledge of the energy gradient of the cross section or of the  $S$  factor is necessary

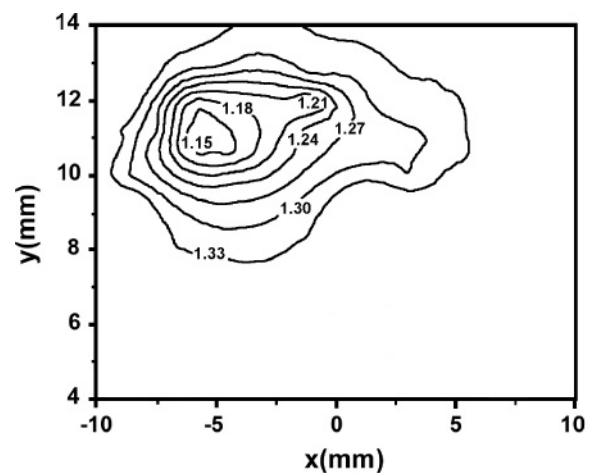


FIG. 9. Typical contours of the number of  $^{12}\text{C}$  atoms in units of  $10^{18}$  atoms per  $\text{cm}^2$  after bombardment. Curves are deduced from interpolation of results of the RBS scan of the target.

for the calculation of the effective reaction energy because only with a nearly constant cross section will all target layers contribute uniformly. With a positive gradient, the larger the gradient, the more it is that only the target layers near the front surface contribute much to the measured  $\gamma$ -ray yield, and the effective target thickness is reduced by this effect. These effects can be simulated, and the effective target thickness and effective reaction energy can be calculated with sufficient accuracy.

From RBS measurements at different positions on the target, an average depth profile was determined for each target. The energy loss in the target for each beam energy used for the  $^{12}\text{C}(\alpha, \gamma)^{16}\text{O}$  cross-section measurements was calculated with TRIM-2000 [46]. These calculations took into account the depth-dependent stoichiometry of  $^{12}\text{C}$  and Au determined in the RBS measurements. Outside the narrow  $E2$  resonance at 2.68 MeV, the effective c.m. energy was calculated by convoluting the depth-dependent  $\alpha$  energy and reaction probability over the target thickness, using the spatially averaged  $^{12}\text{C}$  depth profile and assuming a constant  $S$  factor for the cross-section energy dependence. A constant cross section was assumed for the estimation of the limiting value and the uncertainty in  $E_{\text{c.m. eff.}}$ . The result of the  $S$ -constant calculation is given, in Sec. IV, in column (I) of Tables I and II.

In the narrow  $E2$  resonance region, because of the rapid variation of the  $S$  factor, such a simple treatment can be done only as a limiting value of the effective c.m. energy. In such a situation, when a Breit-Wigner (B-W) function dominates the  $E2$  cross-section variation, an effective c.m. energy can be determined by the convolution of the energy loss with an appropriate weighting function: a pure B-W energy dependence for the  $E2$  resonance plus a constant  $S$  factor for the  $E1$  contribution was used over the whole target thickness to calculate  $E_{\text{c.m. eff.}}$  (see results in column (II) of Tables I and II). However, because of the lack of precise knowledge of the excitation function over the resonance and because the target thickness was much larger than the resonance width, an extreme value of  $E_{\text{c.m. eff.}}$  was also calculated using the same approximations as outside the  $E2$  resonance region, namely, either a constant  $S$  factor or a constant cross section for both contributions. In the resonance region, the two assumptions of constant  $S$  factors [tabulated in col. (I)] and of constant cross sections gave  $E_{\text{c.m. eff.}}$  values differing by less than the 2 keV beam energy resolution. The B-W-dependent and the constant  $S$ -factor results have to be considered as limits to the effective c.m. energy value. With the real target thickness setting a large lower bound on the energy resolution of the experiment, it was not possible to determine  $E_{\text{c.m. eff.}}$  any more precisely in this work. The necessary resonance parameters have been taken from Tilley *et al.* [47]. This procedure was used on the low-energy tail of the narrow  $E2$  resonance. In the falling high-energy tail, the larger corrections due to the asymmetric  $^{12}\text{C}$  depth distribution did not allow the effective c.m. energy to be determined by this method. Because of the difficulty in evaluating the effective c.m. energies, the results for the falling-tail points are not reported in this paper.

A knowledge of the  $^{12}\text{C}$  depth profile in the gold layers is fundamental for the calculation of the  $S$  factors,

for the reduction of the uncertainties associated with the  $^{12}\text{C}$  concentration, and for the calculation of effective c.m. energies which are relevant to the excitation function. The RBS measurements showed that the main consequence of  $\alpha$  bombardment is a modification of the depth profile mainly due to carbon diffusion in the gold layer (see Fig. 7) during the  $^{12}\text{C}(\alpha, \gamma)^{16}\text{O}$  measurements. Thus, the mean energy calculated from the carbon depth profiles inside and outside the beam impact region gives a good estimate of the time- and space-averaged energy loss and of the effective energies in the target before and after bombardment. Because of the dominance of the energy loss in gold, this calculation considers the effective energy as being determined by the  $^{12}\text{C}$  depth profile rather than simply by the number of  $^{12}\text{C}$  atoms under the beam, and consequently it depends both on the implantation procedure of these atoms in the target and on the bombardment history. These secondary effects are taken into account when calculating the uncertainties associated with the effective energies.

To give some examples, for an energy near the  $1^-$  resonance where the assumption of a constant  $S$  factor is valid, the effective c.m. energy is 58 keV less than the uncorrected c.m. energy, which is  $E_{\text{c.m.}} = 2325$  keV for  $E_{\alpha, \text{lab}} = 3100$  keV, yielding  $E_{\text{c.m. eff.}} = 2267$  keV. In this case, a rather thick target was used. For the data points near the narrow  $2^+$  resonance (see Table I), much thinner targets were used. For a data point at  $E_{\alpha, \text{lab}} = 3500$  keV, well below the resonance, the effective c.m. energy, considering the gradient of the  $S$  factor, is  $E_{\text{c.m. eff.}} = 2607$  keV, 18 keV less than the uncorrected value of  $E_{\text{c.m.}}$ . For a data point on the low-energy tail of the  $2^+$  resonance, the constant  $S$ -factor assumption is no longer valid. Using a B-W cross-section energy gradient for the  $E2$  component, and a constant  $E1$   $S$  factor, the energy shift of 18 keV is reduced to 11 keV, yielding  $E_{\text{c.m. eff.}} = 2659$  keV for  $E_{\alpha, \text{lab}} = 3560$  keV.

The uncertainties in the effective c.m. energy and the average amount of  $^{12}\text{C}$  are based on the RBS measurements made in the region of the target marked by the intense  $\alpha$ -particle beam as well as outside this region. They also took into account information about the target homogeneity as discussed in detail in the following. In estimating the uncertainty  $\delta N(^{12}\text{C})$  in the average number of  $^{12}\text{C}$  atoms, we considered the target depth profiles and evaluated the effect of the uncertainty in the beam position for each spectrum. For the thinner targets used above  $E_{\text{c.m.}} = 2.4$  MeV to measure the neighborhood of the narrow  $E2$  resonance, the loss of  $^{12}\text{C}$  under the beam impact showed an uncertainty less than about 10%, calculated considering the accumulated charge. For the thicker targets, the total uncertainty in the average number of  $^{12}\text{C}$  atoms was estimated to be 14%. In the calculation of the effective c.m. energy uncertainty  $\delta E_{\text{c.m. eff.}}$ , above and below the  $E2$  resonance, two terms were considered and added quadratically: the difference between the effective c.m. energies within two regions of the target (inside and outside the beam spot) obtained with the constant  $S$ -factor approximation, and the difference between the  $S$ -constant value and the value obtained using a constant cross-section approximation. The last term is dominant only for the two data points at the lowest energies.

#### IV. RESULTS AND DISCUSSION

In the data analysis, only the radiative capture component to the ground state has been evaluated. For this, the number of detected photons in the full energy peak was obtained by simple integration, where the choice of the integration limits was guided by visual evaluation or, in difficult cases, by comparison with simulated  $\gamma$ -ray spectra to locate the position and width of the peak. Figure 5 shows the full energy peak is clearly visible at high beam energy. For these conditions, the variations with energy and angle of the position and width of the observed peak were in good agreement with the expected position and width evolutions due to the target thickness, the incident beam energy variation, and the Doppler shift. At low  $\alpha$  energy, the expected positions and widths were calculated for each beam energy and detector angle to locate precisely the position and width of the expected peak. For each integration, the background obtained with the pure gold layer at the same energy and with the same target was subtracted from the total number of counts. The net yields for all data points were determined independently by two people in different laboratories, and their results were all in agreement.

The estimation of the errors in the net extracted yields were determined in the standard way from the yield estimates of the total and background counts. At low bombarding energy, when the peak positions were not always visually clear, and to take account of any small variation in the detector energy calibration, an additional contribution to the error was calculated by varying slightly the position and width of the window around the expected values.

In this experiment, we have not evaluated the cascade  $\gamma$  lines, which are at much lower  $\gamma$ -ray energies, because the background was too large at these energies. For the contribution of these weak branches, we refer to the previous works [9,10,16,17,35].

By analyzing the experimental angular distributions (some examples are plotted in Fig. 10 as full points), the parameters  $\sigma_{E1}$ ,  $\sigma_{E2}$  and optionally the phase angle  $\phi_{12}$  between the  $E1$  and  $E2$  capture components can be obtained. From a mathematical point of view, three or four data points in the angular distribution would be sufficient to determine these parameters. However, since the data points are subject to uncertainties, one needs redundant information on the angular distribution.

The values of  $\sigma_{E1}$ ,  $\sigma_{E2}$  and sometimes  $\phi_{12}$  were extracted by a least-squares fit to the measured angular distributions by taking into account the interference between  $E1$  and  $E2$  transitions according to the relation given by Dyer and Barnes [14], here modified for practical purposes as

$$\begin{aligned} \frac{d\sigma}{d\Omega} = \frac{\sigma_{\text{tot}}}{4\pi} & \left[ (3|A_{E1}|^2 + 5|A_{E2}|^2) Q_0 P_0(\cos\vartheta) \right. \\ & + \left( \frac{25}{7}|A_{E2}|^2 - 3|A_{E1}|^2 \right) Q_2 P_2(\cos\vartheta) \\ & - \frac{60}{7}|A_{E2}|^2 Q_4 P_4(\cos\vartheta) + 6\sqrt{3}|A_{E1}||A_{E2}| \\ & \left. \times \cos\phi_{12}(Q_1 P_1(\cos\vartheta) - Q_3 P_3(\cos\vartheta)) \right], \quad (4.1) \end{aligned}$$

where  $\sigma_{\text{tot}}$  is the total cross section (the sum of the  $E1$  and  $E2$  parts),  $d\sigma/d\Omega$  being the corresponding angular differential cross section;  $P_l(\cos\vartheta)$  is the Legendre polynomial of order  $l$ , and  $\vartheta$  is the angle at which the  $\gamma$  rays are observed in the center-of-mass system. It is obtained by transforming  $\vartheta_{\text{lab}}$  into  $\vartheta_{\text{c.m.}}$ . The  $Q_l$  are the attenuation factors of the angular distribution which are due to the finite solid angle of the detector, and  $\phi_{12}$  is the phase angle between the  $E1$  and  $E2$  capture components,  $A_{E1}$  and  $A_{E2}$  being their respective amplitudes. In our setup, displayed in Figs. 2 and 3, each germanium detector was a right circular cylinder with the axis pointed toward the source of the detected  $\gamma$  rays, and with a very slight conical modification to the front part of three of the detectors. The attenuation factors  $Q_l$  [48,49] were calculated according to

$$\begin{aligned} Q_l &= \frac{P_{l-1}(\cos\alpha) - \cos\alpha P_l(\cos\alpha)}{(l+1)(1-\cos\alpha)}, \quad (4.2) \\ \alpha &= \arctan \frac{r}{d+l/2}, \end{aligned}$$

where  $r$  denotes the radius of the detector crystal,  $l$  its length, and  $d$  the real distance between the beam spot and the center of the front face of the crystal.

For the circular cylinder detectors, the  $Q_l$  values are  $0.989 \pm 0.002$ ,  $0.968 \pm 0.004$ ,  $0.936 \pm 0.008$ , and  $0.895 \pm 0.014$  for  $l=1-4$ , respectively. The error bars take into account the various positions, lengths, and radii of the detectors and can be neglected when compared to the error bars of the yields. Differences in  $Q$  introduced by the tapered part of some germanium detectors and by the cryostat window were found negligible at the studied energies and were not taken into account.

The fitting procedure was to first introduce the relevant attenuation factors  $Q_l$  into the theoretical expressions and then to fit the theory to the measured angular distributions. From these results, theoretical angular distributions (plotted as full or dashed lines in Fig. 10) were calculated for the purpose of producing the figures where the effects of finite geometry are thus taken into account in the comparison of the fit to the measurements (see data points of Fig. 10).

Transforming Eq. (4.1) yields

$$\begin{aligned} \frac{d\sigma}{d\Omega} &= \frac{\sigma_{\text{tot}}}{4\pi} W(\cos\vartheta) \\ &= \frac{\sigma_{E1}}{4\pi} W_{E1}(\cos\vartheta) + \frac{\sigma_{E2}}{4\pi} W_{E2}(\cos\vartheta) \\ &\quad + \frac{\sqrt{\sigma_{E1}\sigma_{E2}}}{4\pi} \cos\phi_{12} W_{12}(\cos\vartheta), \quad (4.3) \end{aligned}$$

with

$$\begin{aligned} W_{E1}(\cos\vartheta) &= Q_0 P_0 - Q_2 P_2(\cos\vartheta), \\ W_{E2}(\cos\vartheta) &= Q_0 P_0 + \frac{5}{7} Q_2 P_2(\cos\vartheta) - \frac{12}{7} Q_4 P_4(\cos\vartheta), \\ W_{12}(\cos\vartheta) &= \frac{6}{\sqrt{5}} (Q_1 P_1(\cos\vartheta) - Q_3 P_3(\cos\vartheta)). \quad (4.4) \end{aligned}$$

The relations between the amplitudes  $A_{Ei}$  and partial cross section  $\sigma_{Ei}$  are

$$\frac{\sigma_{E1}}{\sigma_{\text{tot}}} = 3|A_{E1}|^2, \quad (4.5)$$

and

$$\frac{\sigma_{E2}}{\sigma_{\text{tot}}} = 5|A_{E2}|^2. \quad (4.6)$$

The above expression for  $W(\cos \vartheta)$  was fitted using the parameters  $\sigma_{E1}$ ,  $\sigma_{E2}$ , and  $\phi_{12}$ . Barker proposed fixing the phase  $\phi_{12}$  by using the  $\alpha$ -elastic scattering phase shifts [50]. The relationship between  $\phi_{12}$  and the  $\alpha$ -elastic scattering phase shifts  $\delta_1$  and  $\delta_2$  is given by Barker and Kajino [51] as

$$\phi_{12} = \delta_2 - \delta_1 + \arctan(\eta/2), \quad (4.7)$$

where  $\eta$  is the Sommerfeld parameter. This relationship was used to determine the values of  $\phi_{12}$  (given later in Table I) for the two-parameter fits (mentioned below and presented as full lines in Fig. 10) to the experimental angular distributions.

In principle, the formulas (4.1) and (4.3) to (4.7) are only applicable at one energy or for the case of similar variations in  $\sigma_{E1}$  and  $\sigma_{E2}$ , and a constant  $\phi_{12}$  in the energy range of the effective target thickness. The determination of  $\sigma_{E1}$ ,  $\sigma_{E2}$  and  $\phi_{12}$  using the above expression for  $W(\cos \vartheta)$ , which was done in previously published works [9,14,17,20] using  $^{12}\text{C}$  targets, is a first approximation which assumes that the energy loss in the real target is negligible. In the energy range below the  $1^-$  resonance at 2.42 MeV, the energy dependence of  $\sigma_{E1}$  and  $\sigma_{E2}$  are similar enough to not significantly affect the extracted cross-section values even with the thickest targets. At higher energy and outside the  $E2$  resonance at 2.68 MeV, the target thicknesses were also thin enough with respect to the cross-section variations. On the low-energy tail of the  $E2$  resonance, the effective target thickness was even thinner than the physical target thickness. This is why the above formalism was used in the present work for both of the analyses described below. The effect of the residual differences between  $\sigma_{E1}$  and  $\sigma_{E2}$  on the results was checked [30] and is accounted for in the quoted uncertainties of  $\sigma_{E1}$  and  $\sigma_{E2}$ . At this stage of the fitting procedure,  $(d\sigma)/(d\Omega)$ ,  $\sigma_{E1}$ , and  $\sigma_{E2}$  had only a relative normalization for each angular distribution.

The absolute cross sections for the  $E1$  and  $E2$  transitions were then calculated from the angular distribution fits (examples are shown in Fig. 10) by taking into account the integrated beam charge striking the target and the time- and space-average of the total number of carbon atoms in the beam spot. The instantaneous number of  $^{12}\text{C}$  atoms/cm<sup>2</sup> in the beam,  $\bar{N}_{12\text{C}}(t)$ , was determined from the  $^{12}\text{C}$  depth profiles assuming that the loss of carbon atoms is proportional to the accumulated charge on the target. Previous measurements showed such a linear dependence with this type of target [35].  $\bar{N}_{12\text{C}}(t)$  can be written as

$$\bar{N}_{12\text{C}}(t) = \bar{N}_i - (\bar{N}_i - \bar{N}_f) \frac{Q(t)}{Q_f}, \quad (4.8)$$

where  $\bar{N}_i$  is the average target amount of  $^{12}\text{C}$  atoms/cm<sup>2</sup> after production of the target and measured at the border of the target layer not hit by the beam.  $\bar{N}_f$  is the average amount of  $^{12}\text{C}$  atoms/cm<sup>2</sup> at the end of all irradiations, and it was measured in the zone of the beam spot. So  $(\bar{N}_i - \bar{N}_f)$  gives the total loss of carbon at the end of all irradiations.  $\bar{N}_i$  and  $\bar{N}_f$  were deduced from the RBS depth profiles and averaged over the relevant RBS points.  $Q_f$  denotes the total accumulated charge on the target and  $Q(t)$  is the accumulated charge at time  $t$ .

For the thickest targets, made at Bochum University, the implantation process was inhomogeneous and resulted in an enhanced  $^{12}\text{C}$  concentration in the central region of the target. In the evaluation after the experiment, it was difficult to determine precisely the number  $\bar{N}_i$  from the RBS measurements of the  $^{12}\text{C}$  atoms performed outside the region marked by the  $\alpha$ -particle beam. In these cases, only the number  $\bar{N}_f$  of  $^{12}\text{C}$  atoms lying inside the region marked by the  $\alpha$ -particle beam was accurately taken into account. Only estimated limits could be set on  $\bar{N}_i$ , which resulted in larger uncertainties in the effective c.m. energies and in the number of bombarded  $^{12}\text{C}$  atoms.

From the determination of the average number of target atoms/cm<sup>2</sup> and from the target profile, the energy loss and the effective reaction energy were deduced. Also, the uncertainty of this effective energy was estimated (Sec. III). From the effective energy in the laboratory system, the effective c.m. energy was finally calculated for use in Tables I and II and Figs. 11–14 and for calculating the  $S$  factors.

To determine the yield uncertainties of each angular distribution data point, statistical uncertainties in the yields including background subtraction have been added quadratically to the relative uncertainty of the detector efficiencies (Sec. II D). Absolute cross-section uncertainties  $\delta\sigma$  have been obtained by statistical error propagation using CERN's MINUIT package. The estimated uncertainties  $\delta E_{\text{c.m. eff.}}$  were considered statistical, arguing that in most of the cross-section measurements more than one target was used for one energy.

Recently, the experimental data of Ouellet *et al.* [20] were reevaluated by Brune [52] and values of the astrophysical factors  $S_{E1}$  and  $S_{E2}$  have been calculated, first by fixing  $\cos \phi_{12}$  in Eq. (4.1) and then by taking it as a free parameter. This procedure has shown that fixing the phase  $\phi_{12}$  reduces the uncertainties on  $S_{E2}$ . While the values obtained for  $S_{E1}$  differ very little, the  $S_{E2}$  values differ by up to 3 keV b. Some authors [9,53] fit the experimental angular distribution data by using only two free parameters,  $\sigma_{E1}$  and  $\sigma_{E2}$ , while others have considered three free parameters for the fitting [14,17,20]. In the latter case, the extracted phase might be considered as an effective phase which takes into account the target profile and the energy loss of the  $\alpha$ -particle beam in the target, but it might also be understood as affected by unwanted correlations between  $E1$  and  $E2$  amplitudes in the fitting procedure [52]. The calculations of Brune influenced us to treat our new data in both ways and to compare the results.

In the present work, the data have been fitted by applying both procedures: one using three parameters  $\sigma_{E1}$ ,  $\sigma_{E2}$ , and

TABLE I. Final results of the present  $^{12}\text{C}(\alpha, \gamma)^{16}\text{O}$  experiment for the  $E1$  and  $E2$  capture  $\gamma$ -ray cross sections and their relative phase  $\phi_{12}$ .  $E_{\alpha,\text{lab}}$  is the uncorrected  $\alpha$ -particle energy;  $E_{\text{c.m. eff.}}$  is the effective c.m. energy calculated as explained in the text for the two considered cases: (I) using constant  $S$  factors for  $E1$  and  $E2$  contributions to calculate the tabulated value and constant cross sections to calculate a limiting value contribution to the uncertainty; (II) a limiting value of  $E_{\text{c.m. eff.}}$  calculated using a pure Breit-Wigner  $E2$  resonance for the  $E2$  contribution and a constant  $S$  factor for the  $E1$ . For the two-parameter fit, the phase  $\phi_{12}$  was fixed according to Eq. (4.7) with the phases taken from elastic scattering [31,32]. The corresponding  $\chi^2$  values are reduced values for seven degrees of freedom (nine angles and two free parameters for the fit). For the three-parameter fit, the phase was determined according to Eq. (4.1) solely from the data of this experiment. The  $\chi^2$  is the reduced value for six degrees of freedom (nine angles and three free parameters for the fit).

$E_{\alpha,\text{lab}}$ (MeV)	$E_{\text{c.m. eff.}}$ (MeV)		2-parameter fit, phase fixed				3-parameter fit, phase free			
	(I)	(II)	$\sigma_{E1}$ (nb)	$\sigma_{E2}$ (nb)	$\phi_{12}$ (deg)	$\chi^2$	$\sigma_{E1}$ (nb)	$\sigma_{E2}$ (nb)	$\phi_{12}$ (deg)	$\chi^2$
1.850 (2)	1.310(40)		0.19(5)	0.039(34)	54.4(20)	2.4	0.12(4)	0.14(4)	81(6)	1.1
1.900 (2)	1.340(40)		0.16(6)	0.15(6)	54.0(20)	2.0	0.16(4)	0.17(4)	68(5)	1.3
2.300 (2)	1.666(14)		1.39(22)	0.36(9)	49.9(20)	6.4	1.13(19)	0.73(14)	69(3)	3.2
2.700 (2)	1.965(9)		5.4(8)	0.80(14)	40.4(20)	2.8	5.0(7)	1.24(24)	53(3)	1.5
2.800 (2)	2.040(8)		7.8(11)	1.09(21)	35.9(20)	1.4	7.3(11)	1.6(4)	47(5)	1.1
2.900 (2)	2.116(7)		13.4(19)	0.90(18)	29.9(20)	2.3	12.3(18)	2.1(5)	54(4)	1.3
3.000 (2)	2.192(7)		22.7(33)	0.90(17)	20.5(20)	3.1	20.5(30)	3.1(8)	59(4)	1.4
3.050 (2)	2.230(7)		26.7(38)	1.07(20)	13.8(20)	3.7	24.5(36)	3.3(9)	55(5)	2.9
3.100 (2)	2.267(6)		38 (6)	1.59(29)	6.0(20)	1.4	37 (5)	3.1(11)	43(10)	1.3
3.200 (2)	2.343(6)		42 (6)	1.00(21)	13.0(20)	5.2	41 (6)	1.5(12)	38(28)	6.2
3.300 (2)	2.455(3)		35.5(25)	1.88(29)	43.3(20)	2.9	36.6(26)	1.01(15)	0(36)	2.8
3.450 (2)	2.578(2)		20.7(24)	2.2(7)	69.1(20)	2.8	19.8(24)	3.1(10)	75(4)	3.0
3.500 (2)	2.607(3)		19.0(17)	2.2(5)	73.4(20)	5.4	18.2(17)	3.0(6)	79(2)	5.6
3.550 (2)	2.645(3)	2.651(3)	13.0(15)	9.6(12)	78.0(20)	1.6	13.0(15)	9.6(12)	78(2)	1.9
3.560 (2)	2.652(3)	2.659(3)	12.1(13)	11.6(13)	78.7(20)	1.2	12.1(13)	11.6(13)	80(2)	1.4
3.565 (2)	2.656(3)	2.665(3)	12.4(19)	16.2(20)	79.1(20)	2.6	12.4(19)	16.2(20)	80(3)	3.1
3.570 (2)	2.660(3)	2.671(3)	11.1(16)	44 (4)	79.5(20)	1.2	11.2(16)	44 (4)	80(2)	1.4
3.575 (2)	2.663(3)	2.676(3)	10 (4)	192 (18)	79.8(20)	1.4	10 (5)	192 (18)	80(6)	1.7
3.580 (2)	2.667(3)		12 (4)	283 (26)	80.2(20)	2.1	12 (5)	283 (26)	80(5)	2.4
3.600 (2)	2.682(3)		9.8(31)	455 (40)	81.6(20)	7.4	7.8(35)	457 (40)	74(7)	8.3
3.630 (2)	2.705(3)		9.0(19)	76 (7)	83.4(20)	3.2	10.0(20)	75 (7)	90(3)	3.1
3.650 (2)	2.720(3)		6.2(13)	26.7(28)	84.4(20)	4.8	6.4(13)	27.0(28)	90(4)	5.1
3.670 (2)	2.735(3)		6.6(13)	10.8(15)	85.4(20)	1.9	6.6(13)	10.8(15)	86(4)	2.2
3.700 (2)	2.757(3)		5.9(8)	4.1(7)	86.6(20)	1.8	5.8(8)	4.4(7)	93(3)	1.3
3.730 (2)	2.780(3)		6.3(9)	3.3(7)	87.6(20)	1.8	6.2(9)	3.4(7)	90(3)	1.9

$\phi_{12}$  and the other using two parameters, where the phase was fixed by the use of the phase shifts obtained by elastic  $\alpha$ -scattering measurement [31,32]. The work of Tischauser *et al.* [25] could not be used directly because the phase shifts  $\delta_1$  and  $\delta_2$  are not listed in that paper. However, the parameters obtained in their  $R$ -matrix analysis could be compared, and the agreement with the former results of Plaga *et al.* [31] is quite good. Hence, the phase shifts of Plaga were used, as well as those of D'Agostino Bruno *et al.* [32] for the higher energies.

Fixing the phase, one can obtain good fits to the angular distribution data for energies above  $E_{\alpha,\text{lab}} = 2.700$  MeV. Figure 10 shows six typical angular distributions with the fits obtained for both cases: fixed (solid line) and free (dashed line) phase. The characteristics of  $E1$  and  $E2$  capture and their interferences can be seen clearly. At most energies, the differences between the two fitting cases are rather small. Simulations of the angular distributions have shown that the

criteria for fitting the phase are less sharp than for the  $E1$  and  $E2$  amplitudes. As mentioned above, it is difficult to tell whether the differences between the fitted- and the fixed-phase results are due to the fitted phases corresponding to effective phases insofar as they include various uncorrected physical effects, e.g., the variation in phase throughout the whole target thickness and neglect of the effect of any resonance interferences, for example, or are due to the unwanted coupling between the  $E1$  and  $E2$  components in the fitting process.

The  $E1$  and  $E2$  phase differences  $\phi_{12}$  from the three-parameter fits are presented in Fig. 11 for comparison with results obtained by Redder *et al.* [17] and Ouellet *et al.* [20], and with the fixed phase obtained from the elastic scattering phase shifts [31,32]. While the fixed phase values show a cusplike behavior at about  $E_{\text{c.m.}} = 2.3$  MeV, one observes that the values of  $\phi_{12}$  obtained from all the three-parameter fits are lying systematically higher, and the sharp dip near

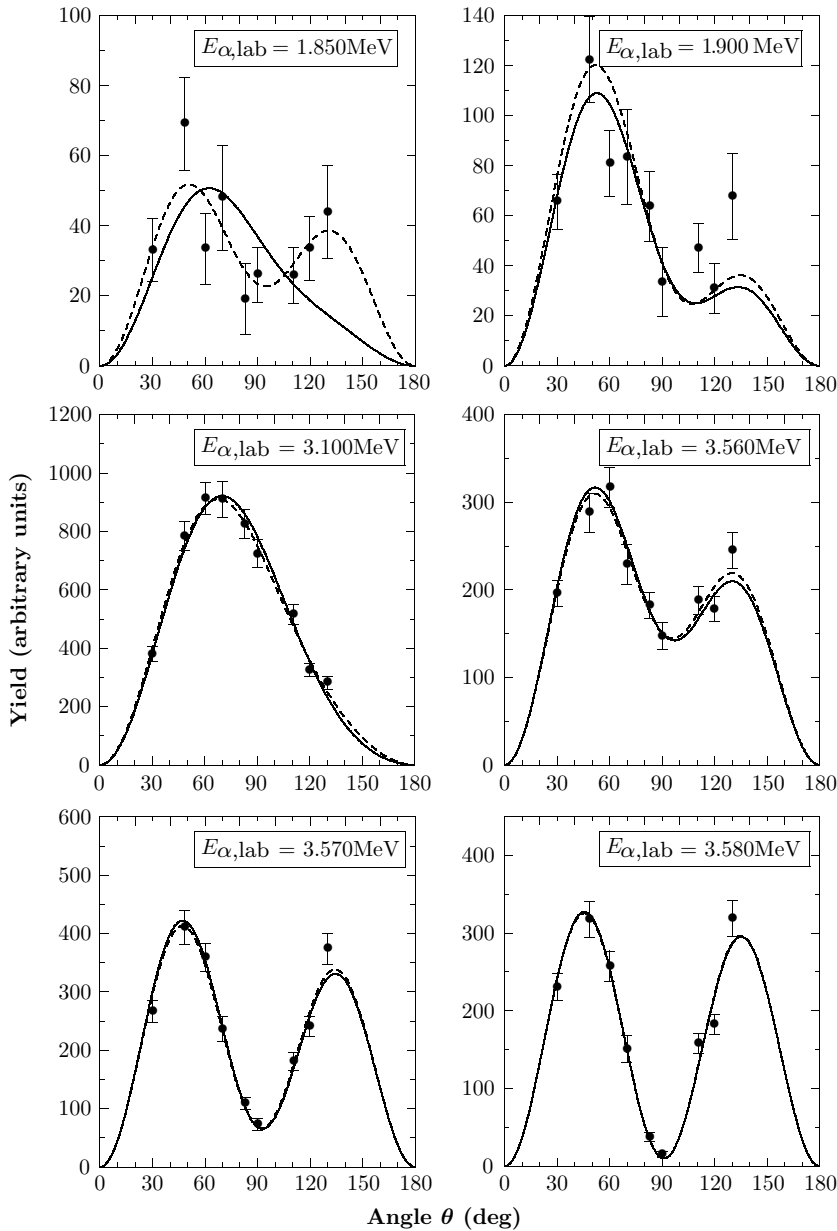


FIG. 10. Examples of six  $\gamma$ -ray angular distributions of the reaction  $^{12}\text{C}(\alpha, \gamma)^{16}\text{O}$  covering nearly the whole energy range of this experiment. Energies are given in the laboratory system. Curves represent the fit of the angular distributions using Legendre polynomials and show clearly the behavior of the angular distribution with  $E1$ ,  $E2$  and the interference from the mixing of both. For these examples, both cases, described in the text, are given: phase  $\phi_{12}$  fixed with the values given in the sixth column of Table I (full line) and as a free parameter yielding the values listed in the tenth column of Table I (dashed line).

the  $1^-$  resonance is missing or smeared out. This smearing occurs, because the fitted phase from the angular distributions corresponds to the mean value of the phase variation over the target thickness and because the uncertainties in the measured data propagate into both the fitted  $E1$  and  $E2$  cross sections and the phase difference. The elastic  $\alpha$ -scattering experiments, with much thinner targets, can determine the detailed energy dependence of  $\phi_{12}$  much more precisely.

These results are also given numerically in Table I where the cross-section values  $\sigma_{E1}$ ,  $\sigma_{E2}$  and the phase  $\phi_{12}$  are tabulated vs the incident  $\alpha$ -particle energy for the two described methods (phase as a fixed or a free parameter). Results of the three-parameter fit can be compared to the previously published ones [14,17,20], while the two-parameter fit was

also used in Ref. [9]. The reduced  $\chi^2$  values are reported for the best fit to the measured angular distributions and will allow the calculation of the limits given by the experiment on the extrapolation of the  $S$  factors at low energies. The effective c.m. energies are also given over the whole energy range. In the energy range of the  $E2$  resonance, two effective energies are given as limiting values, as was discussed in Sec. III.

The  $S$  factors were calculated from the fitted cross-section values  $\sigma_i$  and the effective c.m. energies using the formula given by Rolfs and Rodney [54] and are given in Table II. Outside the narrow  $E2$  resonance at 2.68 MeV, the  $S$  factors were calculated with the effective c.m. energy given in column (I) of Table I considering a constant  $S$  factor for the cross-section dependence as described in Sec. III. In the

TABLE II. Astrophysical  $S$  factors for the  $^{12}\text{C}(\alpha, \gamma)^{16}\text{O}$  reaction obtained from the angular distribution fits. Same  $E_{\text{c.m. eff.}}$  as in Table I.

$E_{\alpha\text{lab}}$ (MeV)	$E_{\text{c.m. eff.}}$ (MeV)		$Q(\text{C})$	$\bar{N}(10^{18} \text{ cm}^{-2})$	2-parameter fit, phase fixed		3-parameter fit, phase free	
	(I)	(II)			$S_{E1}(\text{keV b})$	$S_{E2}(\text{keV b})$	$S_{E1}(\text{keV b})$	$S_{E2}(\text{keV b})$
1.850 (2)	1.310(40)		19.49	11(1)	17(6)	3(3) <sup>a</sup>	11(5)	12(5) <sup>a</sup>
1.900 (2)	1.340(40)		26.54	11(1)	11(5)	10(5) <sup>a</sup>	11(4)	12(4) <sup>a</sup>
2.300 (2)	1.666(14)		30.23	6.6(9)	19(3)	5(1) <sup>a</sup>	16(3)	10(2) <sup>a</sup>
2.700 (2)	1.965(9)		31.39	6.0(8)	25(4)	3.7(7) <sup>a</sup>	23(4)	6(1) <sup>a</sup>
2.800 (2)	2.040(8)		10.19	6.0(8)	29(4)	4.0(8) <sup>a</sup>	27(4)	6(1) <sup>a</sup>
2.900 (2)	2.116(7)		5.78	6.0(8)	39(6)	2.6(5) <sup>a</sup>	36(5)	6(2) <sup>a</sup>
3.000 (2)	2.192(7)		7.25	6.0(8)	54(8)	2.1(4) <sup>a</sup>	49(7)	7(2) <sup>a</sup>
3.050 (2)	2.230(7)		4.87	6.0(8)	57(8)	2.3(4) <sup>a</sup>	53(8)	7(2) <sup>a</sup>
3.100 (2)	2.267(6)		3.67	6.0(8)	74(11)	3.1(6) <sup>a</sup>	71(11)	6(2) <sup>a</sup>
3.200 (2)	2.343(6)		4.33	6.0(8)	67(10)	1.6(3) <sup>a</sup>	66(10)	2(2) <sup>a</sup>
3.300 (2)	2.455(3)		15.16	1.55(10)	44(3)	2.3(4) <sup>a</sup>	45(3)	1.3(2) <sup>a</sup>
3.450 (2)	2.578(2)		12.84	0.55(6)	20(2)	2.1(7) <sup>a</sup>	19(2)	3(1) <sup>a</sup>
3.500 (2)	2.607(3)		21.81	1.36(11)	17(2)	2.0(5) <sup>a</sup>	16(2)	2.7(6) <sup>a</sup>
3.550 (2)	2.645(3)	2.651(3)	6.77	1.32(11)	11(1)	7.9(10) <sup>b,c</sup>	11(1)	7.9(10) <sup>b,c</sup>
3.560 (2)	2.652(3)	2.659(3)	10.02	1.33(11)	10(1)	9.4(11) <sup>b,c</sup>	10(1)	9.4(11) <sup>b,c</sup>
3.565 (2)	2.656(3)	2.665(3)	3.23	1.33(11)	10(2)	13.1(17) <sup>b,c</sup>	10(2)	13.1(17) <sup>b,c</sup>
3.570 (2)	2.660(3)	2.671(3)	4.90	1.34(11)	9(1)	35.5(34) <sup>b,c</sup>	9(1)	35.4(34) <sup>b,c</sup>
3.575 (2)	2.663(3)	2.676(3)	0.62	1.33(11)	8(3)	153(16) <sup>b,c</sup>	8(4)	153(16) <sup>b,c</sup>
3.580 (2)	2.667(3)	...	0.69	1.34(11)	10(3)	...	10(4)	...
3.600 (2)	2.682(3)	...	2.17	1.35(11)	8(2)	...	6(3)	...
3.630 (2)	2.705(3)	...	2.52	1.32(11)	7(1)	...	7(1)	...
3.650 (2)	2.720(3)	...	2.36	1.32(11)	4.4(9)	...	4.6(9)	...
3.670 (2)	2.735(3)	...	3.16	1.32(11)	4.6(9)	...	4.6(9)	...
3.700 (2)	2.757(3)		9.01	1.30(11)	3.9(5)	2.7(4) <sup>a</sup>	3.8(5)	2.9(5) <sup>a</sup>
3.730 (2)	2.780(3)		7.66	1.29(11)	4.0(6)	2.1(4) <sup>a</sup>	4.0(6)	2.2(4) <sup>a</sup>

<sup>a</sup>Calculations with cross sections tabulated in Table I and  $E_{\text{c.m. eff.}}$  (I).<sup>b</sup>Calculations with cross sections tabulated in Table I and  $E_{\text{c.m. eff.}}$  (I) and (II) to get central and limiting values (for I and II: see text and Table I caption). The average of these two values is tabulated, though they are almost identical.<sup>c</sup>Values and error bars take into account uncertainties in the procedure to determine the  $E_{\text{c.m. eff.}}$  value used.

low-energy tail of the narrow  $E2$  resonance where the B-W cross section clearly dominates the cross-section variation, the  $S$  factors were calculated with the  $E_{\text{c.m. eff.}}$  values from columns (I) and (II) of Table I. As the two results had negligible differences, only one value is given in Table II. Although the different  $E_{\text{c.m. eff.}}$  values do not significantly affect the  $E2$   $S$  factors, they will noticeably affect the energy gradient of the  $E2$   $S$  factors, i.e.,  $S_{E2}$  vs  $E_{\text{c.m. eff.}}$ . Finally, the astrophysical  $S$ -factor uncertainties  $\delta S$  were calculated taking into account the uncertainties in the cross section and in the effective c.m. energy as well as the effect of the various possible  $S$ -factor variations on the effective c.m. energy.

The astrophysical  $S$  factors are shown in Fig. 12 for both methods of analysis of the angular distributions. For  $S_{E1}$  the differences between the two methods are rather unspectacular, though the three-parameter values are generally lower below the peak of the  $1^-$  resonance. For  $S_{E2}$  the values obtained with  $\phi_{12}$  as a free parameter are higher, especially in the energy region below the peak of the  $1^-$  resonance. From a mathematical point of view, these higher  $S_{E2}$  values are correlated with the high  $\phi_{12}$  values through Eq. (4.3), where high  $\phi_{12}$  values give a small cosine which is compensated for

by an enlargement of  $\sigma_{E2}$  with  $\sigma_{E1}$  being changed equally in the opposite direction. So the question is reduced to: Why are the  $\phi_{12}$  values higher than those obtained from elastic scattering? Is it a physical effect coming in particular from the  $^{12}\text{C}$  profiles in the real targets, a consequence of the nonlinear character of the third term in Eq. 4.3 or merely the consequence of insufficient sensitivity in fitting  $\phi$ ? To test the latter case, corresponding to the three-parameter fit, some simulations were performed which showed that the higher  $\sigma_{E2}$  values, especially for  $E_{\text{c.m. eff.}}$  between 2.0 and 2.4 MeV, reflect the fact that  $\sigma_{E2}$ ,  $\sigma_{E1}$ , and  $\phi_{12}$  cannot be extracted as independent quantities in such types of  $^{12}\text{C}$  target measurements.

The numerical values of the  $S$  factors  $S_{E1}$  and  $S_{E2}$  are listed in Table II for the two methods of analysis (phase fixed or free). In the low-energy tail of the narrow  $E2$  resonance, the effective c.m. energy is somewhat uncertain, as shown in columns (I) and (II) of Tables I and II, due to the rapid variation of the  $E2$  cross-section contribution as described in Sec. III. Nevertheless, it was found that this uncertainty had a negligible effect on the calculated  $E2$   $S$  factors and their uncertainties, and hence only one value is given in Table II.

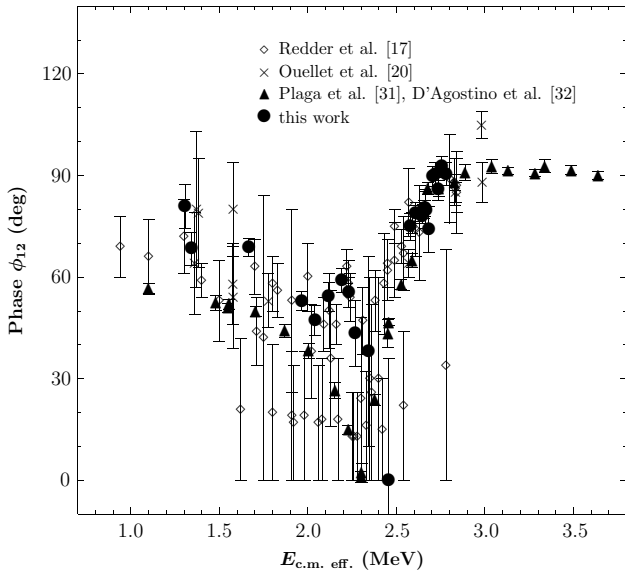


FIG. 11. Energy dependence of phase angle  $\phi_{12}$ , representing the phase difference between  $E1$  and  $E2$   $\gamma$  transitions in the angular distributions corresponding to Eq. (4.1). Results obtained from the three-parameter fit are given as full circles. In comparison, results from the literature also obtained from a three-parameter fit are reported with those shown as full triangles and determined according to Eq. (4.7) and from elastic scattering results of Refs. [31,32].

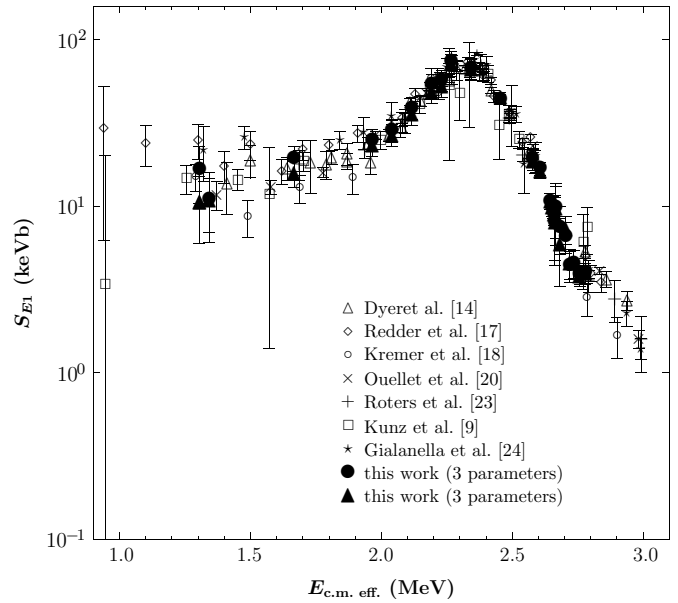


FIG. 13. Comparison of  $S_{E1}$  obtained in this work with values from the literature.

In Fig. 13, the  $S$  factor  $S_{E1}$  is compared to values from the literature, which are scattered at low energy.  $S_{E2}$  is shown in Fig. 14 together with data from the literature. These comparisons underscore the much lower uncertainties in the present experimental determinations.

It should be pointed out that the type of fitting procedures used will definitely influence the results. In our case, the angular distributions were fitted using Eqs. (4.1)–(4.4), thus enforcing the formally correct physical functions. However, if for instance, one were to fit the excitation functions at a fixed angle first, this would not ensure the appropriate physical

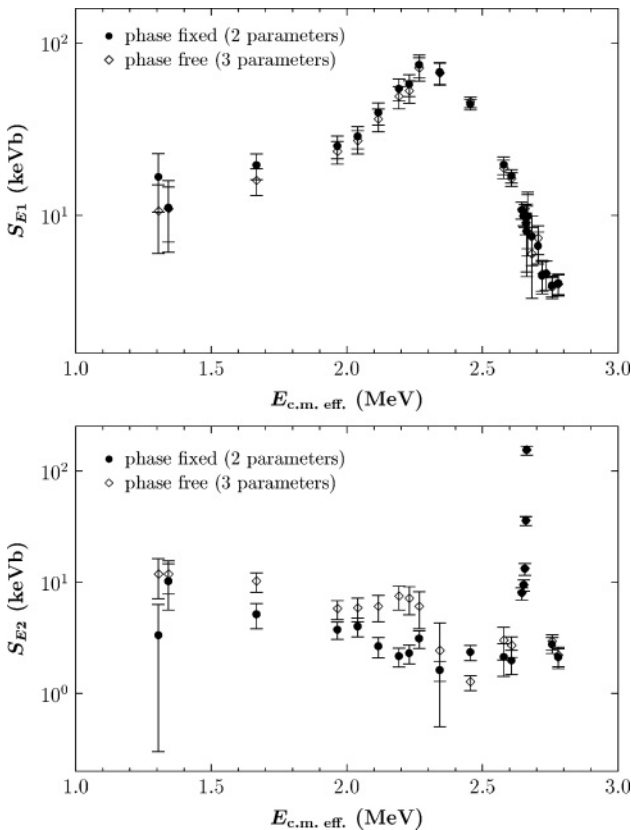


FIG. 12. Astrophysical  $S$  factors for  $E1$  (upper plot) and  $E2$  (lower plot) capture for the  $^{12}\text{C}(\alpha, \gamma)^{16}\text{O}$  reaction obtained in this work.

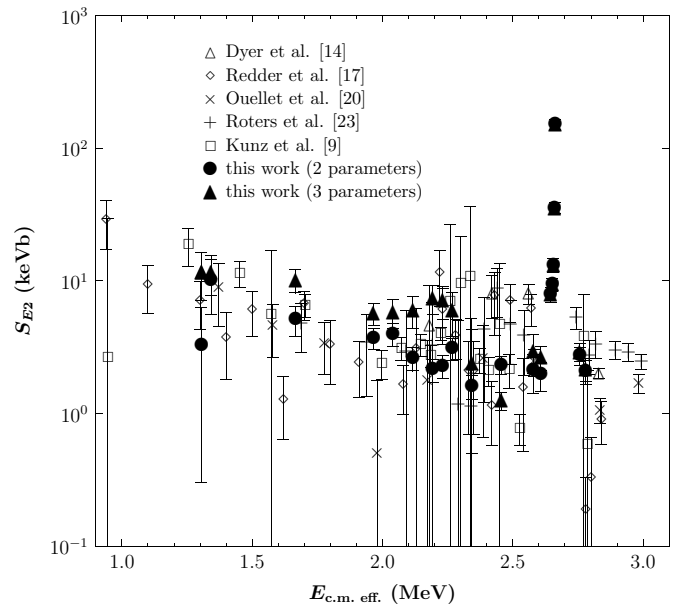


FIG. 14. Comparison of  $S_{E2}$  obtained in this work with values from the literature.

functions for the angular distributions and would consequently lead to different extrapolated values for the  $S$  factors.

## V. CONCLUSION

This study presents new data on the  $^{12}\text{C}(\alpha, \gamma)^{16}\text{O}$  reaction, aiming at a better determination and good separation of the partial cross sections for  $E1$  and  $E2$  capture in the energy range accessible to experiments. In order to improve on the precision and reliability of the previous data, a special effort was made to optimize all essential experimental aspects with today's available techniques. The outstanding characteristic of this experiment was the simultaneous use of nine HPGe detectors in a  $4\pi$  geometry to measure, for the first time in a single run, the complete angular distribution of the emitted  $\gamma$  rays. The HPGe detectors were individually shielded by BGO detectors which reduced the background by a large factor, as can be seen from Fig. 4. It was also important to produce isotopically pure  $^{12}\text{C}$  targets by ion beam implantation and to provide intense  $^4\text{He}$  beams, which were supplied by the DYNAMITRON accelerator of the University of Stuttgart. Good quality data could thus be taken in the energy range  $E_{\text{c.m.}} = 1.305\text{--}2.780$  MeV. Angular-distribution and background measurements were performed during a long beam time period of 3 months.

A particular characteristic of these new measurements is a relatively low background contribution from cosmic rays, which were effectively suppressed, and also a rather low contribution from the beam-induced background, mainly caused by neutron interactions close to the detector. This suppression was possible because of the high depletion factor of  $^{13}\text{C}$  in the target and the low contamination and good vacuum in the beam line. Secondly, the effect of the target  $^{12}\text{C}$  depth profiles on the effective c.m. energy was clearly and precisely determined. The depth profiles of the target were systematically determined by RBS and used to calculate the average number of  $^{12}\text{C}$  atoms/cm<sup>2</sup> in the beam and the effective beam energy. Target analysis is extremely important in this kind of measurement since it is one of the principal sources of systematic uncertainties associated with the cross section. Errors in the effective c.m. energy cause errors in the deduced cross-section energy dependence because of the slope of the excitation function, where the cross section varies roughly by an order of magnitude in a 300 keV interval. The shortcomings of the present experiment were the smaller beam currents of about 100–340  $\mu\text{A}$  compared to the former experiment of Redder *et al.* [17], where the currents at the same accelerator were in the range of 700–800  $\mu\text{A}$ , and the limited measuring time.

Angular distributions of the  $^{12}\text{C}(\alpha, \gamma)^{16}\text{O}$  reaction were measured at nine angles ranging from  $30^\circ$  to  $130^\circ$ . This allowed a precise determination of the respective  $E1$  and  $E2$  contributions to the capture cross section and their relative phase, all of which are reported in Table I together with the best values of the  $\chi^2$ . We have extracted astrophysical  $S$  factors from the two different fits to the angular distributions; first with a fixed relative phase between the  $E1$  and  $E2$  components, taken from the  $^{12}\text{C} + \alpha$  elastic scattering data [31,32], and

second with the relative phase as a free parameter. The results of both methods are presented in Fig. 12 and Table II for the benefit of possible future compilations. From the physical point of view, one should give preference to the two-parameter fitting, but the data of the three-parameter fit are subject to further discussion, following the suggestion in the article of Brune [52].

As can be seen in Figs. 13 and 14, both the  $E1$  and  $E2$   $S$  factors were determined in a more systematic way and with smaller uncertainties than those from previous measurements performed by Dyer and Barnes [14], Redder *et al.* [17], Kremer *et al.* [18], Ouellet *et al.* [19,20], Roters *et al.* [23], and Gialanella *et al.* [24]. The agreement within the limits of uncertainty with the measurements of Kunz *et al.* [9,35] is good. There is also a reasonable agreement in the determination of the phase  $\phi_{12}$  by the three-parameter fit if one compares it to previous determinations by Redder *et al.* [17] and Ouellet *et al.* [20], who also extracted the phase from angular distributions.

The progress achieved since previous measurements is clearly visible for the  $E2$  contribution over the whole energy range studied and particularly in the energy region around the  $E1$  resonance, where the low  $E2$ -to- $E1$  ratio results in an angular distribution strongly dominated by the dipole character. The deviation from an  $E1$  distribution could, however, be determined in our experiment because of the precise data at the nine angles. Redundancy in the data is indispensable in this kind of experiment, which is performed at the limit of sensitivity. All angular distribution fits gave unambiguously the relative  $E1$  and  $E2$  components, with the exception of the lowest energy, where two alternative fits for the two-parameter case yielded different values with a similar  $\chi^2$ . In Tables I and II, only the case with a slightly lower  $\chi^2$  seemed physically realistic and is tabulated. The reason why the differences in the  $S_{E2}$  results between the two procedures (fixed and free phases) are so large remains an open question.

In this paper, we have underlined the importance of a detailed knowledge of the target and the need for target analyses using the highest standards and care available. From the depth profiles, one obtains the information required to calculate the effects of target thickness and to correct the cross-section values properly within the limits of uncertainty. We wish to note, however, that although considerable technical advances were made in this experiment which led to much improved results, the need to use finite target thicknesses still gives limits, especially in the region of the narrow  $E2$  resonance. This is why in order to account as well as possible for those effects, we have chosen to quote two limiting values of  $E_{\text{c.m. eff.}}$  in the region where the shape of the  $E1$  and  $E2$  excitation functions differ considerably.

These new data will certainly be helpful in further constraining and improving the  $R$ -matrix fits and will thus allow for a more accurate extrapolation to the astrophysically relevant energy region around 300 keV. This is especially true for the  $E2$  capture cross section, for which our data help to reduce significantly the uncertainty in the studied energy range.  $R$ -matrix calculations that make use of this new information together with the extrapolation of the  $S$  factors to

$E_{c.m.} = 300$  keV are available in Refs. [30,55] and will be presented in a forthcoming paper [56].

### ACKNOWLEDGMENTS

We are indebted to Professor U. Kneissl for supporting this project. We are obliged to P. Aguer for extensive help and advice about this experiment, C. Angulo and P. Descouvemont for communicating numerical results and

for helpful discussions. Our special thanks go to J. Devin and the technical staffs of the DYNAMITRON, ARAMIS, and SIDONIE accelerators without which this experiment would have been impossible. We thank the France-UK (IN2P3/EPSC) Loan Pool for the EUROGAM detectors. We also thank A. Pape for reading and correcting the manuscript. We acknowledge CNPq, Brazilian Government Agency for M. A. support. This work was supported in part by the IN2P3-CNRS and by the Land Baden-Württemberg.

- 
- [1] T. Rauscher, A. Heger, R. D. Hoffman, and S. E. Woosley, *Astrophys. J.* **576**, 323 (2002).
- [2] L. R. Buchmann and C. A. Barnes, *Nucl. Phys. A*, in press, corrected proof, available online 5 February, 2005.
- [3] T. A. Weaver and S. E. Woosley, *Phys. Rep.* **227**, 65 (1993).
- [4] S. E. Woosley, A. Heger, T. Rauscher, and R. D. Hoffmann, *Nucl. Phys.* **A718**, 3c (2003).
- [5] G. E. Brown, A. Heger, N. Langer, C.-H. Lee, S. Wellstein, and H. A. Bethe, *New Astron.* **6**, 457 (2001).
- [6] G. E. Brown, A. Heger, N. Langer, C.-H. Lee, S. Wellstein, and H. A. Bethe, in *Formation and Evolution of Black Holes in the Galaxy*, World Scientific Series in 20th Century Physics, Vol. 33, edited by H. A. Bethe, G. E. Brown, and C.-H. Lee (World Scientific, Singapore, 2003), p. 317.
- [7] M. M. Boyes, A. Heger, and S. E. Woosley (unpublished).
- [8] C. Angulo, M. Arnould, M. Rayet, P. Descouvemont, D. Baye, C. Leclercq-Willain, A. Coc, S. Barhoumi, P. Aguer, C. Grama, C. Rolfs, R. Kunz, J. W. Hammer, A. Mayer, T. Paradellis, S. Kossionides, C. Chronidou, K. Spyrou, S. Degl'Innocenti, G. Fiorentini, B. Ricci, S. Zavatarelli, C. Providentia, H. Wolters, J. Soares, J. Rahighi, A. Shotter, and M. Lamehi Rachti, *Nucl. Phys.* **A656**, 3 (1999).
- [9] R. Kunz, M. Jaeger, A. Mayer, J. W. Hammer, G. Staudt, S. Harissopulos, and T. Paradellis, *Phys. Rev. Lett.* **86**, 3244 (2001).
- [10] R. Kunz, M. Fey, M. Jaeger, A. Mayer, J. W. Hammer, G. Staudt, S. Harissopulos, and T. Paradellis, *Astrophys. J.* **567**, 643 (2002).
- [11] F. Ajzenberg-Selove, *Nucl. Phys.* **A460**, 1 (1986).
- [12] C. Angulo and P. Descouvemont, *Phys. Rev. C* **61**, 064611 (2000).
- [13] R. E. Azuma, L. Buchmann, F. C. Barker, C. A. Barnes, J. M. D'Auria, M. Dombisky, U. Giesen, K. P. Jackson, J. D. King, R. G. Korteling, P. McNeely, J. Powell, G. Roy, J. Vincent, T. R. Wang, S. S. M. Wong, and P. R. Wrean, *Phys. Rev. C* **50**, 1194 (1994); **56**, 1655 (1997).
- [14] P. Dyer and C. A. Barnes, *Nucl. Phys.* **A233**, 495 (1974).
- [15] T. R. Ophel, A. D. Frawley, P. B. Treacy, and K. H. Bray, *Nucl. Phys.* **A273**, 397 (1976).
- [16] K. U. Kettner, H. W. Becker, L. Buchmann, J. Görres, H. Kräwinkel, C. Rolfs, P. Schmalbrock, H. P. Trautvetter, and A. Vlieks, *Z. Phys. A* **308**, 73 (1982).
- [17] A. Redder, H. W. Becker, C. Rolfs, H.-P. Trautvetter, T. R. Donoghue, T. C. Rinckel, J. W. Hammer, and K. Langanke, *Nucl. Phys.* **A462**, 385 (1987).
- [18] R. M. Kremer, C. A. Barnes, K. H. Chang, H. C. Evans, B. W. Filippone, K. H. Hahn, and L. W. Mitchell, *Phys. Rev. Lett.* **60**, 1475 (1988).
- [19] J. M. L. Ouellet, H. C. Evans, H. W. Lee, J. R. Leslie, J. D. MacArthur, W. McLatchie, H.-B. Mak, P. Skensved, J. L. Whitton, X. Zhao, and T. K. Alexander, *Phys. Rev. Lett.* **69**, 1896 (1992).
- [20] J. M. L. Ouellet, M. N. Butler, H. C. Evans, H. W. Lee, J. R. Leslie, J. D. MacArthur, W. McLatchie, H.-B. Mak, P. Skensved, J. L. Whitton, X. Zhao, and T. K. Alexander, *Phys. Rev. C* **54**, 1982 (1996).
- [21] D. Rogalla, Diplomarbeit, Ruhr-Universität Bochum, 1997 (unpublished).
- [22] H.-P. Trautvetter, G. Roters, C. Rolfs, S. Schmidt, and P. Descouvemont, *Nucl. Phys.* **A621**, 161c (1997).
- [23] G. Roters, C. Rolfs, F. Strieder, and H. P. Trautvetter, *Eur. Phys. J. A* **6**, 451 (1999).
- [24] L. Gialanella, D. Rogalla, F. Strieder, S. Theis, G. Gyürki, C. Agodi, R. Alba, M. Aliotta, L. Campajola, A. Del Zoppo, A. D'Onofrio, P. Figuera, U. Greife, G. Imbriani, A. Ordine, V. Roca, C. Rolfs, M. Romano, C. Sabbarese, P. Sapienza, F. Schümann, E. Somorjai, F. Terrasi, and H.-P. Trautvetter, *Eur. Phys. J. A* **11**, 357 (2001); private communication.
- [25] P. Tischhauser, R. E. Azuma, L. Buchmann, R. Detwiler, U. Giesen, J. Görres, M. Heil, J. Hinfefeld, F. Käppeler, J. J. Kolata, H. Schatz, A. Shotter, E. Stech, S. Vouzoukas, and M. Wiescher, *Phys. Rev. Lett.* **88**, 072501 (2002).
- [26] D. Schürmann, A. Di Leva, L. Gialanella, D. Rogalla, F. Strieder, N. De Cesare, A. D'Onofrio, G. Imbriani, R. Kunz, C. Lubritto, A. Ordine, V. Roca, C. Rolfs, M. Romano, F. Schümann, F. Terrasi, and H.-P. Trautvetter, *Eur. Phys. J. A* **26**, 301 (2005).
- [27] C. R. Brune, W. H. Geist, R. W. Kavanagh, and K. D. Veal, *Phys. Rev. Lett.* **83**, 4025 (1999).
- [28] C. R. Brune, J. Daly, R. Detwiler, B. Fisher, W. H. Geist, J. Görres, H. J. Karwowski, R. W. Kavanagh, D. S. Leonard, P. Tischhauser, K. D. Veal, and M. Wiescher, *Nucl. Phys.* **A688**, 263c (2001).
- [29] K.-D. Joos, Diplomarbeit, Universität Stuttgart, 1997 (unpublished).
- [30] M. Fey, Ph.D. thesis, Universität Stuttgart, Germany 2004, URL: <http://elib.uni-stuttgart.de/opus/volltexte/2004/1683/>; M. Fey, R. Kunz, J. W. Hammer, M. Jaeger, A. Mayer, E. Krmpotic, C. Bauer, C. Meyer, S. Harissopulos, T. Paradellis, G. Staudt, F. Haas, P. Papka, K.-L. Kratz, and B. Pfeiffer, *Nucl. Phys.* **A718**, 131c (2003).
- [31] R. Plaga, H. W. Becker, A. Redder, C. Rolfs, H.-P. Trautvetter, and K. Langanke, *Nucl. Phys.* **A465**, 291 (1987).
- [32] M. D'Agostino Bruno, I. Massa, A. Uguzzoni, G. Vannini, E. Verondini, and A. Vitale, *Nuovo Cimento* **27**, 1 (1975).
- [33] J. W. Hammer, H. M. Schüpferling, E. Bergandt, and Th. Pflaum, *Nucl. Instrum. Methods* **128**, 409 (1975).
- [34] J. W. Hammer, B. Fischer, H. Hollick, H. P. Trautvetter, K. U. Kettner, C. Rolfs, and M. Wiescher, *Nucl. Instrum. Methods* **161**, 189 (1979).

- [35] R. W. Kunz, Ph.D. thesis, Universität Stuttgart, 2002, URL: <http://elib.uni-stuttgart.de/opus/volltexte/2003/1266/>.
- [36] J. W. Hammer and W. Nießner, *Kerntechnik* **17**, 477 (1975).
- [37] J. W. Hammer, G. Bulski, W. Grum, W. Kratschmer, H. Postner, and G. Schleußner, *Nucl. Instrum. Methods Phys. Res. A* **244**, 455 (1986).
- [38] R. Kunz, J. W. Hammer, M. Jaeger, K.-D. Joos, A. Mayer, S. Harissopoulos, T. Paradellis, G. Souliotis, and G. Staudt, in *Capture  $\gamma$ -Ray Spectroscopy and Related Topics: 10<sup>th</sup> International Symposium, Santa Fe, New Mexico, Aug. 30–Sept. 3 1999*, AIP Conf. Proc. 529, edited by S. Wender (AIP, New York, 2000), p. 672.
- [39] P. J. Nolan, D. W. Gifford, and P. J. Twin, *Nucl. Instrum. Methods Phys. Res. A* **236**, 95 (1985).
- [40] P. J. Nolan, *Nucl. Phys.* **A520**, 657c (1990).
- [41] P. J. Nolan, F. A. Beck, and D. B. Fossan, *Annu. Rev. Nucl. Part. Sci.* **44**, 561 (1994).
- [42] A. Antilla *et al.*, *Nucl. Instrum. Methods* **147**, 501 (1977).
- [43] C. Chronidou *et al.*, *Eur. Phys. J. A* **6**, 303 (1999).
- [44] A. Mayer, Ph.D. thesis, Universität Stuttgart, 2001 (unpublished).
- [45] M. O. Thompson, GENPLOT and RUMP documentation, 1996, URL: <http://www.genplot.com/doc/index.htm>
- [46] J. F. Ziegler, computer code TRIM, URL: <http://www.research.ibm.com/ionbeams>, now at <http://www.SRIM.org>.
- [47] D. R. Tilley, H. R. Weller, and C. M. Cheves, *Nucl. Phys.* **A564**, 1 (1993).
- [48] M. E. Rose, *Phys. Rev.* **91**, 610 (1953).
- [49] J. L. Black and W. Gruhle, *Nucl. Instrum. Methods* **46**, 213 (1967).
- [50] F. C. Barker, *Aust. J. Phys.* **40**, 25 (1987).
- [51] F. C. Barker and T. Kajino, *Aust. J. Phys.* **44**, 369 (1991).
- [52] C. R. Brune, *Phys. Rev. C* **64**, 055803 (2001).
- [53] L. Buchmann, R. E. Azuma, C. A. Barnes, J. Humblet, and K. Langanke, *Phys. Rev. C* **54**, 393 (1996).
- [54] C. E. Rolfs and W. S. Rodney, *Cauldrons in the Cosmos* (University of Chicago, Chicago, 1988).
- [55] J. W. Hammer, M. Fey, R. Kunz, J. Kiener, V. Tatischeff, F. Haas, J. L. Weil, M. Assuncao, C. Beck, C. Boukari-Pelissie, A. Coc, J. J. Correia, S. Courtin, F. Fleurot, E. Galanopoulos, C. Grama, F. Hammache, S. Harissopoulos, A. Korichi, E. Krmpotic, D. Le Du, A. Lopez-Martens, D. Malcherek, R. Meunier, P. Papka, T. Paradellis, M. Rousseau, N. Rowley, G. Staudt, and S. Szilner, in *22<sup>nd</sup> International Nuclear Physics Conference, Goeteborg, Sweden, Jun. 22–Jul. 02, 2004*, edited by B. Jonson, M. Meister, G. Nyman, and M. Zhukov; *Nucl. Phys.* **A752**, 514c (2005); **A758**, 363c (2005).
- [56] M. Fey *et al.*, to be published.